Investigation of surface/bulk stresses of nanoparticles with diffusive interfaces using the phase field crystal model

Ming-Wei Liu and Kuo-An Wu*
Department of Physics, National Tsing Hua University, 30013 Hsinchu, Taiwan
(Received 2 October 2017; revised manuscript received 23 November 2017; published 15 December 2017)

We investigate the surface stress of solid-liquid diffusive interfaces at equilibrium using the phase field crystal model in two dimensions. To analytically study the surface energy dependence on elastic strains, we employ the amplitude equation formalism and recast the free energy functional in terms of strains and amplitudes of density waves to examine the intricate coupling between them. For planar interfaces, the surface stress and its anisotropy are explored using the phase field crystal model and its amplitude equations. The anisotropy of surface stress is shown to be closely related to the anisotropic density waves across the interface, and a stronger anisotropy is observed in the surface stress than that in the surface energy. In addition, to investigate the curvature effect, we examine resultant strain fields at equilibrium within nanoparticles of various sizes subjected to their surface stresses. The measured strains are compared with the classical sharp interface model. The discrepancy in strain fields arises as the size of nanoparticles becomes smaller which suggests a curvature dependent surface stress for diffusive interfaces. We construct the effective surface stress using the measured strain fields and classical linear elasticity theory. The overall magnitude of the effective surface stress decreases with the radius of the nanoparticle, and the effective surface stress is shown to be more isotropic for small nanoparticles.

DOI: 10.1103/PhysRevB.96.214106

I. INTRODUCTION

In recent studies, it has been shown that the surface stress plays a crucial role in a wide range of material processing applications including nanotube formation [1], surface stress-driven instability in thin films [2], surface reconstruction [3–5], self-assembled monolayers on solid surfaces [6–8] and stability of vapor deposited thin films [9]. The surface stress, as an intrinsic source of stresses applied to the solid nuclei, would genuinely influence both thermal and mechanical equilibrium of solid-liquid systems. Its effects become more pronounced as the curvature of the surface gets larger. Therefore, at the nanoscale, the surface stress is an important determinant influencing the growth of crystals.

As first proposed by Gibbs [10,11], the surface stress is the reversible work done per unit area to stretch the existing surface elastically, in contrast to the interfacial energy which is the reversible work done per unit area to create a new surface. The Shuttleworth equation [12] simply relates the surface stress $\tau_{\alpha\beta}$ and the interfacial energy γ,

$$\tau_{\alpha\beta} = \gamma\delta_{\alpha\beta} + \frac{\partial\gamma}{\partial\tilde{\varepsilon}_{\alpha\beta}}, \tag{1}$$

where $\tilde{\varepsilon}_{\alpha\beta} \equiv \varepsilon_{\alpha\zeta} P_{\zeta\beta}$ represents the projected strain on the surface, and $P_{\alpha\beta} \equiv \delta_{\alpha\beta} - \hat{n}_\alpha \hat{n}_\beta$ is the projection operator which maps the strain tensor onto the surface coordinates in which $\hat{n}$ is the unit normal vector of the interface pointing from solid to liquid. The surface stress is a second rank tensor like the bulk stress but with only two independent components along the interface. It is clear from the Shuttleworth equation that the surface stress is identical to the surface tension and the surface energy for fluid-fluid (liquid or vapor) interfaces since atoms rearrange themselves from interior to the surface as the new surface area is created. However, the surface stress and surface energy would be different for solid-solid or solid-fluid interfaces. Moreover, it is worth noting that while the interfacial energy must be positive for a stable interface, the surface stress could be either positive or negative which corresponds to a compressive or tensile stress at the surface, respectively.

The surface stress of an atomistically smooth solid-vapor interface at low temperature has been studied for various systems including Lennard-Jones crystal [13] and metallic fcc crystals [14–17]. For atomistically rough solid-liquid interfaces, Frolov and Mishin have extensively analyzed the surface stress of copper and its dependence on temperature and bulk stresses using molecular dynamics (MD) simulations [18–20]. Nevertheless, it remains unclear, for nanoparticles with diffusive interfaces, how the surface stress and its anisotropy are affected by the size of the nanoparticle. In this paper, we employ the phase field crystal (PFC) model to explore the properties of the surface stress and its effects on the nanoparticles.

The PFC model is a continuum model that has been used extensively to model materials at atomistic length scale at equilibrium and outside equilibrium. It has its roots in the density functional theory of freezing as discussed in detail in Ref. [21]. The PFC model has been employed to study various fundamental problems including elastic and plastic deformation [22–25], stress-induced morphology of epitaxial films [26–30], crystal nucleation [31–33], nonequilibrium crystal growth [32,34–36], and grain-boundary grooving [37]. Variants of the PFC model are derived for various materials applications such as binary alloys [38,39], liquid crystals [40,41], and ferromagnetic materials [42].

In order to quantitatively analyze the excess properties across the interface where the density waves decay slowly across several lattice planes from solid to liquid, we also employ the amplitude equations (AE) derived from the PFC model. The AE method rests on the multiscale analysis that separates slowly varying amplitude and the underlying density

*kuoan@phys.nthu.edu.tw

waves [43–47]. Therefore, the AE method is suitable to study the diffusive interfaces [48] as well as the crystal morphology at mesoscopic scales [38,39,49]. The deformation of crystal can also be implemented into the AE approach to investigate nonlinear elasticity of crystals [50,51] and the morphological instability of strained films [52].

To quantitatively study the surface stress of a diffusive interface, we calculate the surface stress of a planar interface using the PFC model and AE in two dimensions. In addition, we investigate crystal grains of various sizes immersed in equilibrium with the melt to explore the dependence of surface stress and its anisotropy on the size of nanoparticles. The resultant bulk stress within the nanoparticles due to the surface stress is analyzed and is compared to the classical theory in the sharp interface limit. The discrepancy between the sharp interface model and the PFC model for small nanoparticles due to diffusive interface is discussed in detail.

This paper is organized as follows: In Sec. II, we briefly review the thermodynamic and mechanical equilibrium for a solid-liquid coexistence system. The corresponding strain fields within a circular grain subjected to anisotropic surface energy and surface stress are derived. In Sec. III, we derive amplitude equations from the PFC model and explicitly recast them in terms of the strain fields to investigate the intricate coupling between strains and the excess surface energy of a diffusive interface. In Sec. IV, numerical investigation of the planar surface stress and its anisotropy is discussed. In addition, the comparison of the resultant strain fields within the nanoparticle to the sharp interface model is discussed. Furthermore, the curvature-dependent effective surface stress is analyzed in detail.

II. THERMAL AND MECHANICAL EQUILIBRIUM

A. Thermal and mechanical equilibrium of crystal seeds in two dimensions

In order to quantitatively investigate the equilibrium state of solid-liquid systems, we derive the local equilibrium condition in the limit where the interface is much smaller than the sizes of bulk phases. The free energy functional of a solid-liquid coexistence system in two dimensions is composed of bulk energies and the interfacial energy,

$$F = \int_l da f_l(n_l) + \int_s da f_s(n_s,\boldsymbol{\varepsilon}) + \int_{sl} d\ell\gamma(\theta,\tilde{\boldsymbol{\varepsilon}}), \quad (2)$$

where f_l and f_s are the bulk energy densities of the liquid and solid phases, respectively. Both bulk energy densities depend on the particle number density n, and the solid energy density also depends on the strain tensor $\boldsymbol{\varepsilon}$. The interfacial energy γ varies as a function of the crystal orientation θ as well as the surface strain tensor $\tilde{\boldsymbol{\varepsilon}}$.

The thermal equilibrium conditions are obtained by minimizing the free energy functional with respect to the density and the area of each phase while keeping the total particle number and area conserved. The above-mentioned conditions simply require that the solid and liquid phases have the same chemical potential, μ, and a different pressure for a curved surface due to the surface stiffness, $\gamma + \gamma''$,

$$\Delta\mu = \mu_s - \mu_l = \frac{\partial f_s}{\partial n_s} - \frac{\partial f_l}{\partial n_l} = 0 \quad (3)$$

$$\Delta p = p_s - p_l = (\mu_s n_s - f_s) - (\mu_l n_l - f_l) = \kappa(\gamma + \gamma'') \quad (4)$$

in which κ stands for the curvature of the surface and γ'' denotes the second derivative of the interfacial energy with respect to the crystal orientation, $\gamma'' \equiv \partial^2\gamma/\partial\theta^2$. Note that we have assumed the dependence of surface energy on the curvature is weak and negligible in the derivation. As a consequence, the coexistence densities change with the curvature of the surface of the crystal seed due to the nonvanishing Laplace pressure Δp which results from the balance of the surface stiffness and pressures.

In addition to the thermal equilibrium conditions, the mechanical equilibrium conditions are obtained by minimizing the free energy functional with respect to the bulk strain tensor and the surface strain tensor for the bulk solid and solid-liquid interface, respectively. It gives

$$\boldsymbol{\sigma} \equiv (f_s - n_s\mu_s)\boldsymbol{I} + \frac{\partial f_s}{\partial \boldsymbol{\varepsilon}} = -p_s\boldsymbol{I} + \frac{\partial f_s}{\partial \boldsymbol{\varepsilon}} \quad (5)$$

$$\nabla\cdot\boldsymbol{\sigma} = 0 \quad (6)$$

$$[\boldsymbol{\sigma} + p_l\boldsymbol{I}]\cdot\hat{n} = \frac{d\boldsymbol{\tau}}{d\ell}\cdot\hat{t}, \quad (7)$$

where $\boldsymbol{I}$ is the second rank identity tensor, and $d/d\ell$ is the differential operator along the interface of which $\hat{t}$ is the unit tangent vector.

For a planar interface, of which $\kappa = 0$, μ and p of the solid and liquid phases are equal, and the solid completely relaxes mechanically that gives $\sigma_{nn} = 0$ and $\sigma_{tn} = 0$, where the subscript n (t) denotes the normal (transverse) direction in regard to the interface. As a consequence, for the interfaces in mechanical equilibrium, there is only one component of the surface stress, namely τ_{tt}, that we need to take into account for a two-dimensional solid liquid system, since the shearing of the surface is equivalent to the shearing of the solid in a rotated frame; see Fig. 1.

B. Circular grain of isotropic material

For a circular seed with a constant curvature, $\kappa = 1/R_0$, and isotropic surface energy and surface stress, the equilibrium state can be expressed in a simpler fashion in the polar coordinates, (r,ϕ), in which r and ϕ are the radial and angular coordinates that correspond to the normal and transverse directions with respect to the interface. As a result, the equilibrium conditions are readily

$$\Delta\mu = 0, \qquad \Delta p = \frac{\gamma}{R_0}, \qquad \sigma_{rr} + p_l = -\frac{\tau_{tt}}{R_0}, \quad (8)$$

where the differential of surface stress along the interface, $d\boldsymbol{\tau}/d\ell$, is approximately $-\kappa\hat{n}\tau_{tt}$.

For an elastically isotropic material in two dimensions, the stress-strain constitutive relation is

$$\sigma_{\alpha\beta} = K\delta_{\alpha\beta}\varepsilon_{\zeta\zeta} + 2G\left(\varepsilon_{\alpha\beta} - \frac{1}{2}\delta_{\alpha\beta}\varepsilon_{\zeta\zeta}\right) - p_s\delta_{\alpha\beta} \quad (9)$$

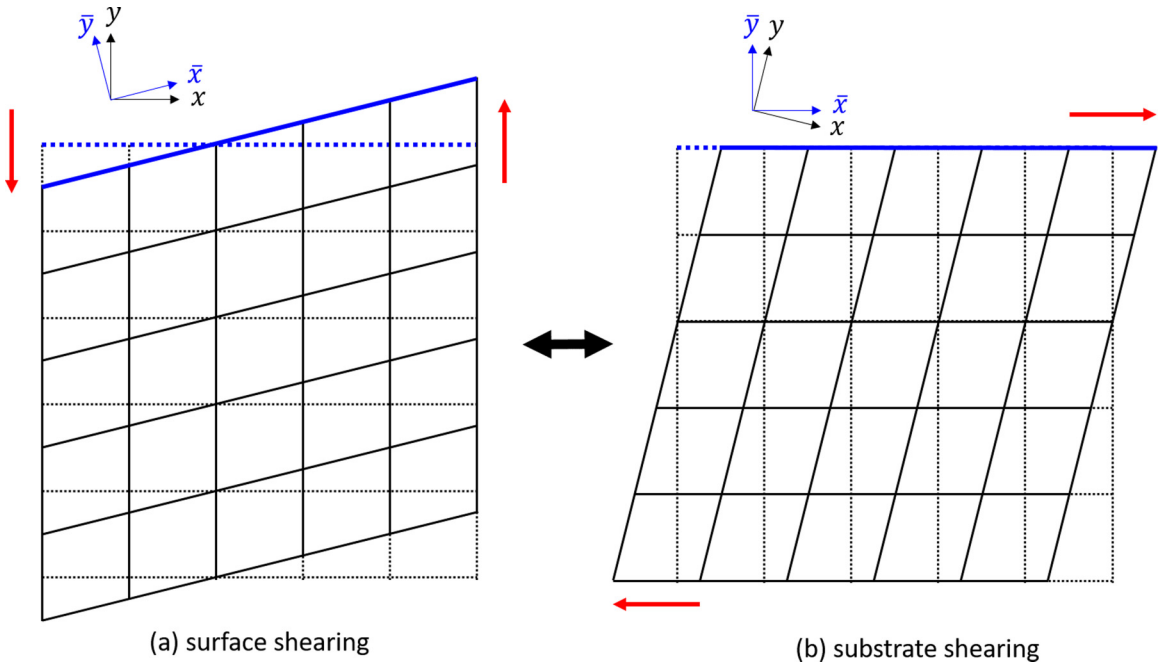

FIG. 1. The surface shearing and the substrate shearing share the same deformation effect on the surface which is indicated in a blue line. The solid line represents the deformed state and the dashed line represents the reference state.

in which K and G are the bulk and the shear moduli, respectively. For a 2D isotropic material, the bulk modulus and the shear modulus are related to the Poisson ratio, $\nu = (K - G)/(K + G)$. We readily obtain the fact that due to the isotropic surface stress the solid undergoes a uniform bulk strain, ε_0, which is inversely proportional to R_0,

$$\varepsilon_{rr} = \varepsilon_{\phi\phi} = \varepsilon_0 \equiv -\frac{\Delta\tau_{tt}}{2K R_0} \tag{10}$$

in which $\Delta\tau_{tt}$ represents the difference between the surface stress and the surface energy, $\Delta\tau_{tt} \equiv \tau_{tt} - \gamma = \frac{\partial\gamma}{\partial\varepsilon_{tt}}$.

C. Anisotropic strain profile

For realistic materials, the surface energy and the surface stress exhibit anisotropy that reflects the underlying crystal symmetry. In the following, we consider hexagonal crystal structures which are commonly observed in 2D systems. The hexagonal lattices are elastically isotropic 2D structures due to the hexagonal symmetry and the elastic properties are determined by only two moduli of elasticity. The anisotropic profiles of the surface energy and the surface stress of hexagonal crystals can be approximately expressed as the series expansion of $\cos 6\theta$ and its harmonics,

$$\gamma(\theta) \cong \gamma^{(0)} + \sum_{m=1}^{\infty} \gamma^{(6m)} \cos(6m\theta) \tag{11}$$

$$\tau_{tt}(\theta) \cong \tau_{tt}^{(0)} + \sum_{m=1}^{\infty} \tau_{tt}^{(6m)} \cos(6m\theta), \tag{12}$$

where the superscript indicates the corresponding harmonics and θ is defined such that the orientation $\theta = 0$ corresponds to the close packed orientation. Note that the surface orientation is set to be equivalent to the angular coordinate, $\theta = \phi$, in the circular seed case.

Together with the equilibrium conditions Eqs. (3), (4), (6), and (7) and the stress-strain constitutive relation for an isotropic material Eq. (9), we derive equilibrium profiles of strain fields within a circular crystal seed of the radius R_0, that is, subjected to the anisotropic surface energy and surface stress as shown in Eqs. (11) and (12),

$$\varepsilon_{rr} = -\frac{\Delta\tau^{(0)}}{2K R_0} + \sum_{m=1}^{\infty}\left[(6m+1)\left(\frac{-1}{2K} + \frac{6m}{4G}\right)\frac{\Delta\tau_1^{(6m)}}{R_0}\rho^{6m} + (6m-1)\left(\frac{-6m}{4G}\right)\frac{\Delta\tau_2^{(6m)}}{R_0}\rho^{6m-2}\right]\cos(6m\phi) \tag{13}$$

$$\varepsilon_{\phi\phi} = -\frac{\Delta\tau^{(0)}}{2K R_0} + \sum_{m=1}^{\infty}\left[(6m+1)\left(\frac{-1}{2K} - \frac{6m}{4G}\right)\frac{\Delta\tau_1^{(6m)}}{R_0}\rho^{6m} + (6m-1)\left(\frac{6m}{4G}\right)\frac{\Delta\tau_2^{(6m)}}{R_0}\rho^{6m-2}\right]\cos(6m\phi) \tag{14}$$

$$\varepsilon_{\phi r} = \sum_{m=1}^{\infty}\left[(6m+1)\left(-\frac{6m}{4G}\right)\frac{\Delta\tau_1^{(6m)}}{R_0}\rho^{6m} + (6m-1)\left(\frac{6m}{4G}\right)\frac{\Delta\tau_2^{(6m)}}{R_0}\rho^{6m-2}\right]\sin(6m\phi), \tag{15}$$

where ρ is the normalized radial coordinate, $\rho \equiv r/R_0$, $\Delta\tau^{(0)} \equiv \tau_{tt}^{(0)} - \gamma^{(0)}$, $\Delta\tau_1^{(6m)} \equiv \tau_{tt}^{(6m)} + (6m-1)\gamma^{(6m)}$, and $\Delta\tau_2^{(6m)} \equiv \tau_{tt}^{(6m)} + (6m+1)\gamma^{(6m)}$. The detailed derivation is shown in Appendix A. It is clear that the strain fields within the solid are more pronounced as the radius of the circular seed gets smaller, since the strain field are inversely proportional to R_0. Besides the $1/R_0$ scaling, the mathematical form of

the strain field within the circular crystal only depends on normalized radial coordinate ρ and the angular coordinate ϕ.

It is clear that the above derived strain fields are only valid in the sharp interface limit. However, for materials with rough interfaces, it remains unclear how the finite interface width would influence the surface stress and the corresponding strain fields. In the following, we employ the phase field crystal approach and its amplitude equations to quantitatively explore the strain fields subject to the anisotropic surface stress of materials with rough interfaces.

III. PHASE FIELD CRYSTAL MODEL

A. Free energy functional

A variety of the PFC model has been proposed in order to generalize the model to describe the various crystal symmetries [53–55]. Here, we restrict our attention to the simplest formulation of PFC since we focus on the relation of surface stress and the underlying crystal symmetry, although the following derivation could be easily generalized for other PFC models.

The dimensionless form of the simplest PFC free energy functional is

$$F = \int d\vec{r}\,\frac{\psi}{2}[-\epsilon + (1+\nabla^2)^2]\psi + \frac{\psi^4}{4} \tag{16}$$

in which ψ serves as the dimensionless particle density difference with respect to a reference state, and ϵ is a control parameter that determines the interfacial properties and elasticity of materials which can be set once the liquid structure factor of the material at the melting point is known [23]. To investigate strain fields of nanocrystal seeds at the solid-liquid equilibrium, we employ the relaxational conserved dynamics,

$$\frac{\partial \psi}{\partial t} = \nabla^2 \mu, \tag{17}$$

where μ is the local chemical potential defined as

$$\mu \equiv \frac{\delta F}{\delta \psi} = [-\epsilon + (1+\nabla^2)^2]\psi + \psi^3. \tag{18}$$

Hence, the chemical potential μ must be a uniform constant over the system when it reaches equilibrium.

The liquid phase is a homogeneous state, $\psi = \bar{\psi}_l$, where $\bar{\psi}_l$ is a constant, and the free energy density is obtained straightforwardly from Eq. (16),

$$f_l = (-\epsilon + 1)\frac{\bar{\psi}_l^2}{2} + \frac{\bar{\psi}_l^4}{4}. \tag{19}$$

In comparison, the solid state could be expressed approximately by a mean density $\bar{\psi}_s$ and a group of density waves that reflects the symmetry of the solid,

$$\psi_s(\vec{r}) \approx \bar{\psi}_s + \sum_j A_j e^{i\vec{K}_j\cdot\vec{r}} + \sum_j A_j^* e^{-i\vec{K}_j\cdot\vec{r}}, \tag{20}$$

where A_j is the amplitude of each density wave and $\vec{K}_j$ is the reciprocal lattice vector (RLV). For small values of ϵ, the solid state at coexistence can be well represented by employing only the set of principal RLVs. For triangular lattices in two dimensions, the principal RLVs are

$$\vec{K}_j = \cos\left(\frac{2\pi j}{3}\right)\hat{x} + \sin\left(\frac{2\pi j}{3}\right)\hat{y} \tag{21}$$

with its counterparts $-\vec{K}_j$, in which j is an integer ranging from 1 to 3. Since the sixfold symmetry of the triangular lattice ensures that all density waves have the same amplitude A_s, the free energy density of the solid is readily derived from Eq. (16),

$$f_s = (-\epsilon + 1)\frac{\bar{\psi}_s^2}{2} + \frac{\bar{\psi}_s^4}{4} - 3\epsilon A_s^2 + 9\bar{\psi}_s^2 A_s^2 + 12A_s^3\bar{\psi}_s + \frac{45}{2}A_s^4. \tag{22}$$

By minimizing the free energy density with respect to A_s, we obtain the amplitude of density waves of the solid phase,

$$A_s = -\frac{\bar{\psi}_s}{5} + \frac{\sqrt{15\epsilon - 36\bar{\psi}_s^2}}{15}, \tag{23}$$

which is coupled to ϵ and $\bar{\psi}_s$. It is shown by Elder and Grant [23] that the elastic constants of crystals are proportional to A_s^2, and later on we will derive the formulas of elastic constants in amplitude equations formalism.

The coexistence densities for solid-liquid systems with planar interfaces are determined by requiring both phases have the same chemical potential and pressure. Detailed calculations are discussed in Refs. [45] and [37]. For small values of ϵ, the coexistence densities can be expressed as a series expansion of $\epsilon^{1/2}$,

$$\bar{\psi}_s \approx \epsilon^{1/2}\psi_{s0} + \epsilon^1\psi_{s1} + \epsilon^{3/2}\psi_{s2} + \mathcal{O}(\epsilon^2) \tag{24}$$

$$\bar{\psi}_l \approx \epsilon^{1/2}\psi_{l0} + \epsilon^1\psi_{l1} + \epsilon^{3/2}\psi_{l2} + \mathcal{O}(\epsilon^2). \tag{25}$$

For hexagonal lattices, the coefficients are computed using the common tangent construction which leads to $\psi_{s0} = \psi_{l0} = \psi_c \equiv -\sqrt{15/37}$, $\psi_{s1} = \psi_{l1} = 0$, and $\psi_{s2} = -\psi_{l2} = 16/(5\sqrt{555})$. Notably, the miscibility gap $\bar{\psi}_s - \bar{\psi}_l$ is proportional to $\epsilon^{3/2}$.

B. Amplitude equations

The amplitude equations are obtained using the multiscale expansion assuming that the amplitude profile varies much more slowly than the underlying periodicity of the crystal. As shown in Refs. [45] and [37], the amplitude of density waves depends on a slow spatial variable $\vec{R} = \epsilon^{1/2}\vec{r}$, and thus, we can express the density field as

$$\psi(\vec{R},\vec{r}) \approx \epsilon^{1/2}\left[\psi_c + \epsilon n(\vec{R}) + \sum_{j=1}^{3} A_j(\vec{R})e^{i\vec{K}_j\cdot\vec{r}} + \sum_{j=1}^{3} A_j^*(\vec{R})e^{-i\vec{K}_j\cdot\vec{r}}\right], \tag{26}$$

where n is the average density over a unit cell. As a consequence, the effective free energy functional with respect

to amplitudes and average density becomes

$$F \cong \epsilon \int d\vec{R} \sum_{j=1}^{3} |\hat{L}_j A_j|^2 + \bar{f}_{\text{local}} + \mathcal{O}(\epsilon^2) \tag{27}$$

$$\hat{L}_j \equiv 2i\vec{K}_j \cdot \nabla_R + \epsilon^{1/2}\nabla_R^2 \tag{28}$$

$$\begin{aligned}\bar{f}_{\text{local}} \equiv{}& (-1+\epsilon^{-1})\frac{\psi_c^2}{2} + \psi_c(-\epsilon+1)n + \epsilon\frac{n^2}{2} + \frac{\psi_c^4}{4} + \epsilon\psi_c^3 n \\ &+ \left(3\psi_c^2 + 6\epsilon\psi_c n - 1\right)\sum_{j=1}^{3}|A_j|^2 + 6(\psi_c + \epsilon n) \\ &\times (A_1A_2A_3 + A_1^*A_2^*A_3^*) + \frac{3}{2}\sum_{j=1}^{3}|A_j|^4 \\ &+ 6\sum_{j=1}^{3}\sum_{k>j}^{3}|A_j|^2|A_k|^2\end{aligned} \tag{29}$$

in which ∇_R denotes the gradient with respect to $\vec{R}$. The second term in Eq. (27) is a nonlinear function of free energy density which simply depends on local density and amplitudes. Furthermore, the amplitudes A_j and average density n follow the nonconserved and conserved relaxational dynamics, respectively,

$$\frac{\partial A_j}{\partial t} = -\frac{\delta F}{\delta A_j^*} = -\hat{L}_j^2 A_j - \frac{\partial \bar{f}_{\text{local}}}{\partial A_j^*} \tag{30}$$

$$\frac{\partial n}{\partial t} = \nabla^2\frac{\delta F}{\delta n} = \epsilon\nabla_R^2\frac{\partial \bar{f}_{\text{local}}}{\partial n}. \tag{31}$$

Due to the dependence of $\hat{L}_j$ on $\vec{K}\cdot\nabla_R$, the profile of amplitudes would vary differently across the interface depending on surface orientation which leads to anisotropic interfacial properties, as shown by Wu and Karma [45].

In bulk phases, n and A_j are uniform and the free energy densities, $\bar{f}_s$ and $\bar{f}_l$, of solid and liquid, respectively, are expressed by $\bar{f}_{\text{local}}(n, A_j)$ with different average density and amplitudes,

$$\bar{f}_s = \bar{f}_{\text{local}}(n_s, \bar{A}), \qquad \bar{f}_l = \bar{f}_{\text{local}}(n_l, 0), \tag{32}$$

where n_s and n_l are the average density of solid and liquid, respectively, and $\bar{A}$ is the common amplitude among the density waves, which corresponds to A_s in PFC, $A_s \cong \epsilon^{1/2}\bar{A}$. The values of n_s, n_l, and $\bar{A}$ at solid-liquid coexistence are solved using $\frac{\partial \bar{f}_s}{\partial \bar{A}} = 0$ and the thermal equilibrium conditions, Eqs. (3) and (4).

C. Solid-liquid interfacial energy

The interfacial energy is the excess free energy of forming an interface [18], and in the PFC model the interfacial energy of a planer interface can be evaluated by the following expression shown in Ref. [45],

$$\gamma = L^{-1}\int d\vec{r}\left[f - \left(\frac{\psi-\bar{\psi}_l}{\bar{\psi}_s-\bar{\psi}_l}f_s + \frac{\psi-\bar{\psi}_s}{\bar{\psi}_l-\bar{\psi}_s}f_l\right)\right], \tag{33}$$

where L is the length of the interface and f represents the free energy density, which is the integrand in Eq. (16). For amplitude equations, the 2D solid-liquid system with a planar interface can be simplified further to a 1D problem due to homogeneity in the direction parallel to the interface. Similar expression of the interfacial energy is derived for AE,

$$\begin{aligned}\gamma = \epsilon^{3/2}\int dZ\Bigg[&\sum_{j=1}^{3}|\hat{L}_j A_j|^2 + \bar{f}_{\text{local}} \\ &- \left(\frac{n-n_l}{n_s-n_l}\bar{f}_s + \frac{n_s-n}{n_s-n_l}\bar{f}_l\right)\Bigg]\end{aligned} \tag{34}$$

in which $\hat{L}_j$ is reduced to one-dimensional form, $\hat{L}_j = (\vec{K}_j\cdot\hat{n})\partial_Z + \epsilon^{1/2}\partial_Z^2$, and Z is along the direction of the interface normal $\hat{n}$.

D. Deformation and strains

1. Deformation

Before deriving surface stress for the PFC model, it is necessary to identify the measure of the deformation such as displacement vector $\vec{u}$ in the PFC model, which has been discussed in Refs. [24,25,38,50]. The deformation could be regarded as a transformation of lattice basis defined as

$$e^{i\vec{K}\cdot\vec{r}} \to e^{i\vec{K}\cdot\vec{r}'} = e^{i\vec{K}\cdot(\vec{r}-\vec{u})} \tag{35}$$

which corresponds to shifting a lattice point $\vec{r}'$ to a new position $\vec{r}$ with a displacement $\vec{u}$. Then, the phase of A_j's is associated with the local displacement field $\vec{u}$. This description works well within bulk solid, where the crystal symmetry is preserved; however, it is not sufficient for the interface region where atoms are subjected to asymmetric interatomic potential. Therefore, an additional phase in the amplitudes is required to completely capture lattice deformations due to asymmetric forces experienced by atoms at the interface. The general form of the amplitude can be expressed as

$$A_j = a_j e^{-i\vec{K}_j\cdot\vec{u}}e^{i\varphi}, \tag{36}$$

where $a_j \equiv |A_j|$ is the magnitude of amplitudes and φ is the mean phase of the three amplitudes, $A_1A_2A_3 = |A_1A_2A_3|e^{3i\varphi}$, which is an additional degree of freedom apart from the displacement vector. For a stress-free solid-liquid system at equilibrium, $\vec{u}$ is homogeneous, and φ vanishes in bulk solid, but both of them vary across the interface and their variations are in the order of ϵ, $\nabla\vec{u} \sim \nabla\varphi \sim \epsilon$, which will be derived in detail below.

With Eq. (36), one can readily quantify the excess free energy contribution due to strains by applying $\hat{L}_j$ to the amplitudes,

$$\begin{aligned}\hat{L}_j A_j &= \hat{L}_j a_j e^{-i\vec{K}_j\cdot\vec{u}+i\varphi} = e^{-i\vec{K}_j\cdot\vec{u}+i\varphi}\hat{L}_j' a_j \\ &\cong e^{-i\vec{K}_j\cdot\vec{u}+i\varphi}(\hat{L}_j + M_j + i\hat{N}_j + G_j + i\hat{H})a_j + \mathcal{O}(\epsilon^2)\end{aligned} \tag{37}$$

$$M_j \equiv 2\epsilon^{-1/2}K_{j\alpha}K_{j\beta}\varepsilon_{\alpha\beta} \tag{38}$$

$$\hat{N}_j \equiv -2K_{j\alpha}u_{\alpha,\beta}\bar{\partial}_\beta - K_{j\alpha}(\bar{\partial}_\beta u_{\alpha,\beta}) \tag{39}$$

$$G_j \equiv -2\epsilon^{-1/2}K_{j\alpha}\varphi_{,\alpha} \tag{40}$$

$$\hat{H} \equiv 2\varphi_{,\alpha}\bar{\partial}_\alpha + (\bar{\partial}_\alpha\varphi_{,\alpha}), \tag{41}$$

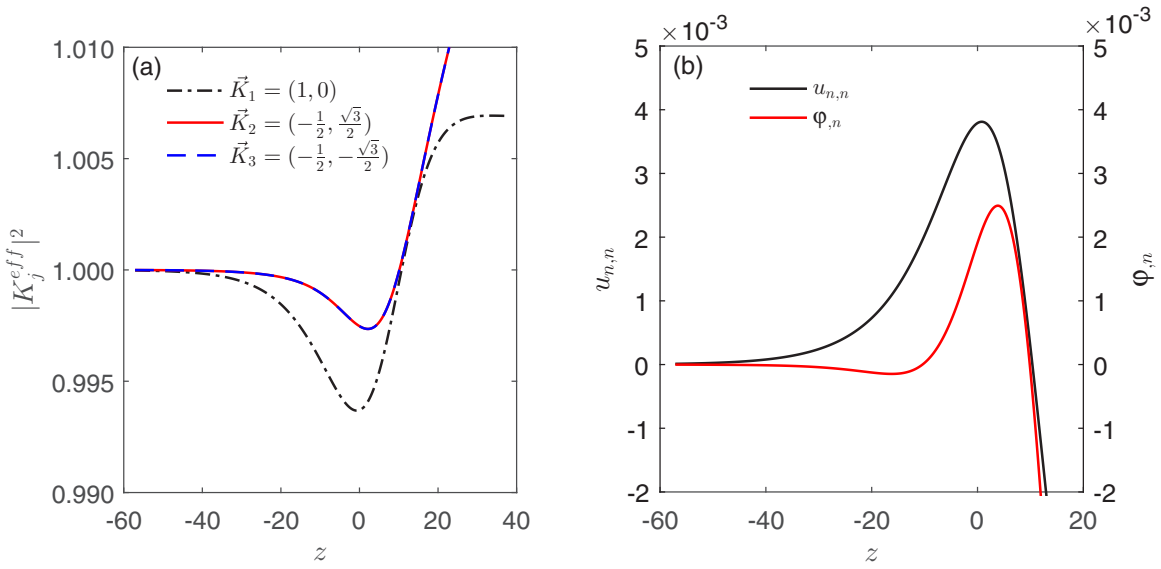

FIG. 2. The profiles of (a) the magnitude squared of effective RLVs, $|K_j^{\text{eff}}|^2$, as well as (b) the normal components $u_{n,n}$ and $\varphi_{,n}$ across the interface for the close packed orientation of which the normal vector of the interface is $\hat{n} = (1,0)$. The interface is located at $z = 0$ and the solid (liquid) is in the negative (positive) regime of z.

where $K_{j\alpha}$ represents the α component of the vector $\vec{K}_j$, ε serves as the strain field, $\varepsilon_{\alpha\beta} \equiv \frac{1}{2}(u_{\alpha,\beta} + u_{\beta,\alpha})$, $u_{\alpha,\beta} \equiv \frac{\partial u_\alpha}{\partial r_\beta}$, $\varphi_{,\beta} \equiv \frac{\partial \varphi}{\partial r_\beta}$, and $\bar{\partial}_\alpha \equiv \frac{\partial}{\partial R_\alpha}$. For a small value of ϵ, we neglect higher order terms of ϵ as well as higher order terms of ε in Eq. (37) in the limit of the diffuse interface and linear elasticity.

2. *Effective RLVs*

The physical interpretation of each term in Eq. (37) can be easily understood by examining the changes in RLVs which are directly associated with $\vec{u}$ and φ. $u_{\alpha,\beta}$ and $\varphi_{,\alpha}$ could be viewed approximately as the change in RLVs given the slow variation of $\vec{u}$ and φ over space. For example, considering a density field including $\vec{u}$ and φ, that is, $\rho(\vec{r}) = \sum_{j=1}^{3} \cos(K_{j\alpha} r_\alpha - K_{j\alpha} u_\alpha + \varphi)$, it is straightforward through Taylor expansion around a reference point at $\vec{r} = 0$ to obtain

$$\begin{aligned}\rho(\vec{r}) &\cong \sum_{j=1}^{3} \cos[K_{j\alpha} r_\alpha - K_{j\alpha}(u_\alpha(0) + \partial_\beta u_\alpha(0) r_\beta) \\ &\quad + (\varphi(0) + \partial_\beta \varphi(0) r_\beta)] \\ &= \sum_{j=1}^{3} \cos[(K_{j\alpha}\delta_{\alpha\beta} - K_{j\alpha} u_{\alpha,\beta}(0) + \varphi_{,\beta}(0)) r_\beta \\ &\quad - K_{j\alpha} u_\alpha(0) + \varphi(0)], \end{aligned} \tag{42}$$

where $u_\alpha(0)$ and $\varphi(0)$ vanish in equilibrium bulk solid. Therefore, the effective RLV is

$$K_{j\beta}^{\text{eff}} \equiv K_{j\alpha}(\delta_{\alpha\beta} - u_{\alpha,\beta}) + \varphi_{,\beta} \tag{43}$$

of which the magnitude squared is

$$\left|\vec{K}_j^{\text{eff}}\right|^2 \cong |\vec{K}_j|^2 - 2K_{j\alpha}K_{j\beta}\varepsilon_{\alpha\beta} + 2K_{j\alpha}\varphi_{,\alpha} \tag{44}$$

in which the last two terms correspond to M_j and G_j, respectively, see Eqs. (38) and (40). Accordingly, M_j and G_j are regarded as the magnitude change of $\vec{K}_j$ due to $\vec{u}$ and φ, respectively, see Fig. 2(a). The equilibrium profiles of $u_{n,n}$ and $\varphi_{,\alpha}$ for planar interfaces of stress-free solid-liquid systems are shown in Fig. 2(b). For planar interfaces, there are intrinsic strains $u_{\alpha,\beta}$ and a nontrivial mean phase φ varying across the interface and the profiles change with the surface orientation. The positive value of $u_{n,n}$ indicates that the lattice expansion occurs in the interface region, which has been observed in MD simulation of the hard-sphere system in three dimensions [56].

Furthermore, the gradient kernel $\hat{L}'_j$ in Eq. (37) could also be recast in terms of $\vec{K}_j^{\text{eff}}$,

$$\begin{aligned}\hat{L}'_j &= \epsilon^{-1/2}\left[\left(1 - \left|K_j^{\text{eff}}\right|^2\right) + 2i\epsilon^{1/2} K_{j\alpha}^{\text{eff}} \bar{\partial}_\alpha + \epsilon \bar{\partial}_\alpha \bar{\partial}_\alpha \right. \\ &\quad \left. + i\epsilon^{1/2}\left(\bar{\partial}_\alpha K_{j\alpha}^{\text{eff}}\right)\right]. \end{aligned} \tag{45}$$

It shows the intricate coupling between the strain fields and density wave profiles which gives rise to the surface stress.

With Eq. (37), we rewrite the free energy functional Eq. (27) in terms of n, a_j, $\vec{u}$, and φ,

$$\begin{aligned}F &= \epsilon \int d\vec{R} \sum_{j=1}^{3} |(\hat{L}_j + M_j + i\hat{N}_j + G_j + i\hat{H}) a_j|^2 \\ &\quad + \bar{f}_{\text{local}}(a_j, n, \varphi), \end{aligned} \tag{46}$$

and the corresponding governing equations for the scalar amplitude a'_js are

$$\frac{\partial a_j}{\partial t} = -2|\hat{L}_j + M_j + i\hat{N}_j + G_j + i\hat{H}|^2 a_j - \frac{\partial \bar{f}_{\text{local}}}{\partial a_j}, \tag{47}$$

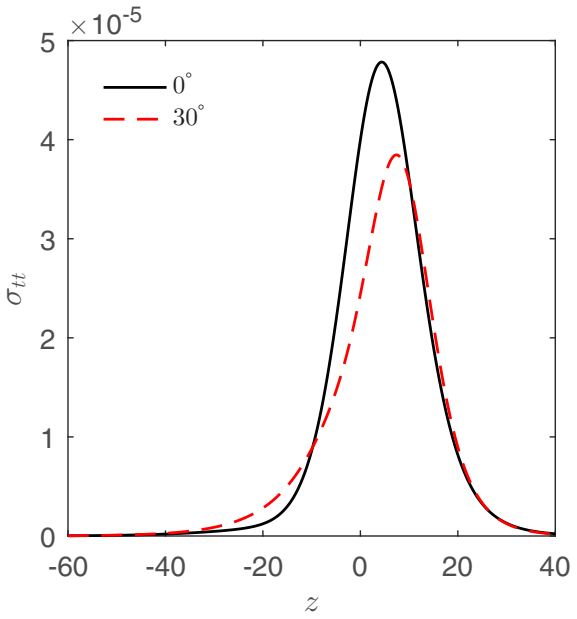

FIG. 3. The profiles of the transverse stress σ_{tt} for two orientations across the interface.

while the governing equation for n remains unchanged. Besides, the evolution equations for $\vec{u}$ and φ are derived accordingly,

$$\frac{\partial u_\alpha}{\partial t} \cong \epsilon^{1/2}\bar{\partial}_\beta\left[\sum_{j=1}^{3}(L_j a_j + M_j a_j)\left(\frac{\partial M_j}{\partial u_{\alpha,\beta}}a_j + i\frac{\partial \hat{N}_j}{\partial u_{\alpha,\beta}}a_j\right) + \text{c.c.}\right] - \epsilon^{1/2}\bar{\partial}_\beta\bar{\partial}_\beta\left[\sum_{j=1}^{3}(L_j a_j)\left(i\frac{\partial \hat{N}_j}{\partial(\bar{\partial}_\mu u_{\alpha,\mu})}a_j\right) + \text{c.c.}\right] + \mathcal{O}(\epsilon^{3/2}) \tag{48}$$

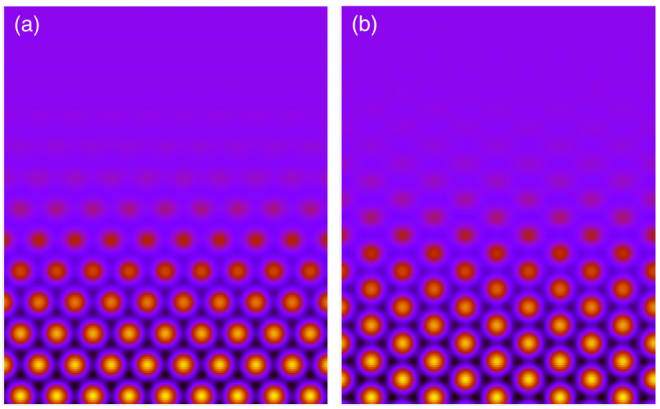

FIG. 4. The snapshots of the solid-liquid interfaces at equilibrium in PFC simulation for two orientations, namely, (a) the close-packed orientation and (b) the zigzag orientation.

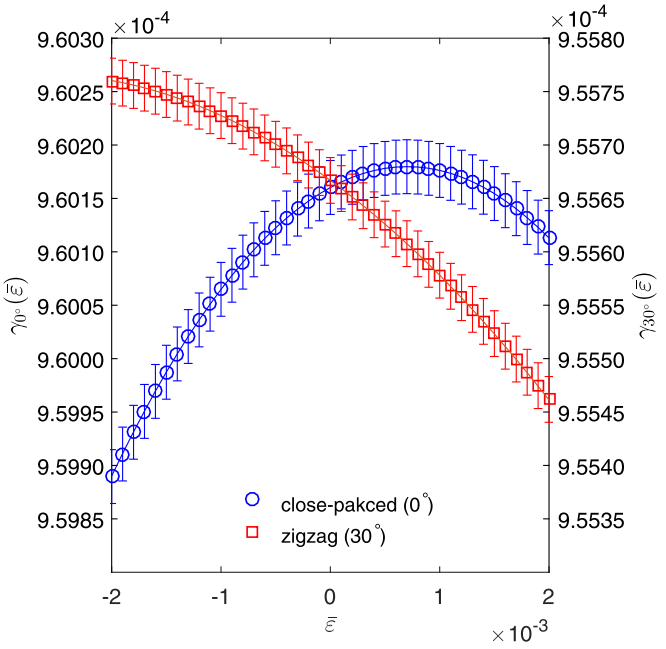

FIG. 5. The excess interfacial energy as function of strains for $\epsilon = 0.1$. The PFC simulation results for 0° (close-packed) and 30° (zigzag) orientations are shown in the blue circles and red squares, respectively. The solid lines are the fitted quadratic curves.

$$\frac{\partial \varphi}{\partial t} \cong \epsilon^{1/2}\bar{\partial}_\beta\left[\sum_{j=1}^{3}(L_j a_j)\left(\frac{\partial G_j}{\partial \varphi_{,\beta}}a_j + i\frac{\partial \hat{H}}{\partial \varphi_{,\beta}}a_j\right) + \text{c.c.}\right] - \epsilon^{1/2}\bar{\partial}_\beta\bar{\partial}_\beta\left[\sum_{j=1}^{3}(L_j a_j)\left(i\frac{\partial \hat{H}}{\partial(\bar{\partial}_\mu \varphi_{,\mu})}a_j\right) + \text{c.c.}\right] - \frac{\partial \bar{f}_{\text{local}}}{\partial \varphi} + \mathcal{O}(\epsilon^{3/2}) \tag{49}$$

in which c.c. denotes the complex conjugate. For bulk solid at equilibrium where the derivatives of a_j vanish and only the term related to $M_j\frac{\partial M_j}{\partial u_{\alpha,\beta}}$ remains, Eq. (48) is reduced to

$$\partial_\beta\left[\sum_{j=1}^{3}2\frac{\partial M_j}{\partial u_{\alpha,\beta}}M_j a_j^2\right] = \partial_\beta\left[\sum_{j=1}^{3}2\frac{\partial M_j}{\partial u_{\alpha,\beta}}\frac{\partial M_j}{\partial u_{\mu,\nu}}a_j^2 u_{\mu,\nu}\right] = \partial_\beta(C_{\alpha\beta\mu\nu}u_{\mu,\nu}). \tag{50}$$

This formula rediscovers the mechanical equilibrium condition in bulk solid for the PFC model under the description of the linear elasticity theory. The similar derivation has been shown by Heinonen *et al.* [25]. The elastic moduli for different crystal symmetries can also be elegantly derived from the above AE formalism, see Appendix B. For 2D triangular lattices, the bulk and shear moduli are calculated, $K = 6\epsilon\bar{A}^2$ and $G = 3\epsilon\bar{A}^2$.

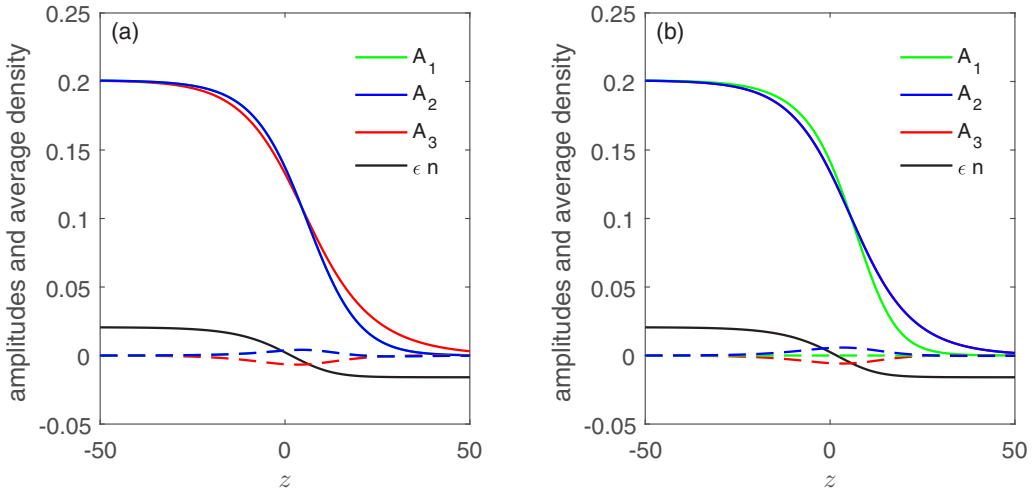

FIG. 6. The profiles of amplitudes for two orientations, (a) the close-packed and (b) the zigzag orientations of which the surface normal $\hat{n}$ are (1,0) and $(\frac{\sqrt{3}}{2}, \frac{1}{2})$, respectively. The real and imaginary parts of the amplitudes are shown in the solid and dashed lines, respectively. Note that $A_1 = A_2$ for the close packed orientation and the real parts of A_1 and A_3 are identical for the zigzag orientation.

E. Surface energy and surface stress

The dependence of the excess interfacial energy on the strains can be shown by substituting Eq. (46) into Eq. (34),

$$\gamma = \epsilon^{3/2} \int dZ \left[\sum_{j=1}^{3} |(\hat{L}_j + M_j + i\hat{N}_j + G_j + i\hat{H})a_j|^2 + \bar{f}_{\text{local}} - \left(\frac{n - n_l}{n_s - n_l} \bar{f}_s + \frac{n_s - n}{n_s - n_l} \bar{f}_l \right) \right]. \quad (51)$$

The expression of the surface stress is readily obtained using the Shuttleworth equation,

$$\begin{aligned} \tau_{tt} &= \gamma + \frac{\partial \gamma}{\partial \varepsilon_{tt}} \cong \gamma + \int dZ \sum_{j=1}^{3} \frac{\partial M_j}{\partial \varepsilon_{tt}} a_j (\hat{L}_j + M_j + G_j) a_j \\ &\quad + \text{c.c.} \\ &= \gamma + \epsilon^{3/2} \int dZ \left[\sum_{j=1}^{3} 4K_{jt}^2 a_j \left(\partial_Z^2 + 2\epsilon^{-1} K_{j\alpha} K_{j\beta} \varepsilon_{\alpha\beta} \right. \right. \\ &\quad \left. \left. - 2\epsilon^{-1} K_{j\alpha} \varphi_{,\alpha} \right) a_j \right]. \end{aligned} \quad (52)$$

It is clear that the surface stress is closely related to the change in the RLVs across the interface as shown above.

In the recent research with MD simulations [19,20], it is discovered that there are nontrivial intrinsic stress fields across the solid-liquid interface in three dimensions. Based on the expression of surface stress in terms of stress fields, $\tau_{tt} = \int dz \sigma_{tt}$, we calculate the corresponding transverse stress σ_{tt} and present the result in Fig. 3. Similar to the result in the MD studies, the stress profile depends on the surface orientation and exhibits an asymmetric profile across the interface rather than the Lorentzian-like distribution proposed by Levitas [57] in phase field theory.

IV. RESULTS AND DISCUSSIONS

A. Surface stresses and its anisotropy

In addition to the above theoretical analysis, we quantitatively investigate the surface stress of solid-liquid interfaces using the PFC model as well as the AE method. The surface stress is calculated for triangular lattices in two dimensions, and its dependence on crystal orientation and the parameter ϵ is examined.

1. PFC simulation

In order to measure the surface stress in the PFC model, we simulate solid-liquid coexistence systems with various prescribed strains and calculate the excess interfacial free energy and its variation with respect to the strains to obtain the surface stress. The simulation of a solid-liquid system consists of an extended solid domain in contact with liquid and periodic boundary conditions are employed in the simulations. Two orientations which are studied extensively in this paper are the close-packed orientation and the zigzag orientation which correspond to $\theta = 0^\circ$ and $\theta = 30^\circ$, respectively, see Fig. 4. To accurately compute the surface stress, it is important to determine a stress-free solid state (i.e., the reference state) numerically. As shown by Wu and Voorhees [26], the length of the RLV would slightly differ from unity and depends on ϵ due to higher harmonics in the density waves. Therefore, based on the two-mode calculation and numerical simulations, we set the RLVs for the stress-free solid to be $\vec{K}_j^o \to (1 - \Delta K)\vec{K}_j$, where $\Delta K = 0.04702\%$ for $\epsilon = 0.1$. The prescribed lateral strain is applied by deforming the RLVs with a strain tensor,

$$\vec{K}_j^a \to \vec{K}_j^o \cdot (\boldsymbol{I} - \bar{\varepsilon} \hat{t} \otimes \hat{t}). \quad (53)$$

As the result, the crystal would be stretched by a uniform strain ($\varepsilon_{tt} = \bar{\varepsilon}$). The excess interfacial energy is computed accordingly using Eq. (33).

These procedures are carried out for various crystal orientations to further compute the anisotropy of the surface stress. The details of setting up dimensions of the periodic simulation

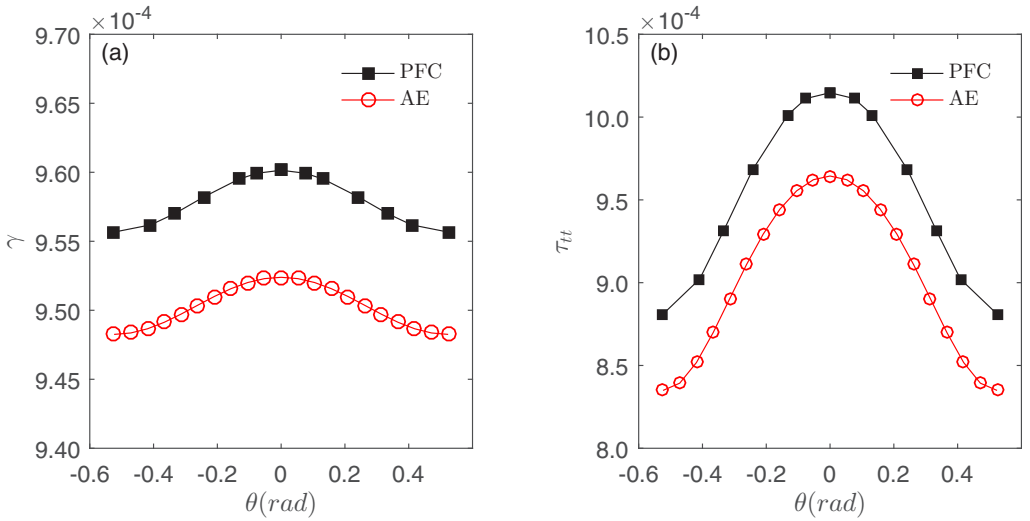

FIG. 7. (a) The surface energy and (b) the surface stress of different orientations for $\epsilon = 0.1$ are obtained from the PFC model (black squares) and the AE model (red circles).

domain for different crystal orientations are discussed in Ref. [58]. Furthermore, in order to prevent the interaction among interfaces, the dimensions of solid and liquid domains parallel to the interfaces normal are 10 times larger than the interface thickness. The interface thickness is about 45.9 in the PFC dimensionless length corresponding to $6.3a_0$ where a_0 is the interatomic spacing ($a_0 \cong 7.3$).

According to the Shuttleworth equation, Eq. (1), the surface stress is calculated using the surface energy and its derivative with respect to $\bar{\varepsilon}$. Our simulation results show that the surface energy changes quadratically with applied stains and this relation also exhibits a strong orientation dependence, see Fig. 5. These observations are consistent with recent MD simulations for Cu [20]. The derivative of the interfacial free energy with respect to $\bar{\varepsilon}$ around $\bar{\varepsilon} = 0$ is positive for the close-packed orientation and negative for the zigzag orientation. Consequently, the surface stress is more anisotropic than the surface energy.

2. AE simulation

The AE simulation of a 2D planar solid-liquid interface is readily reduced to a 1D system, since the order parameters A_j and n are constant along the direction parallel to the interface. The equilibrium profiles of amplitudes and average density vary smoothly across the interface, as depicted in Fig. 6, while in bulk phases A_j and n are constant, $n_l = -0.1586$ for bulk liquid and $n_s = 0.2065$ and $\bar{A} = 0.2008$ for bulk solid. According to Eqs. (34) and (52), the surface energy and the surface stress for strain-free crystals are calculated with the equilibrium profiles of A_j and n.

3. Comparison and results

The orientation dependence of surface energy and surface stress calculated from PFC and AE simulations is presented in Fig. 7. The results from the PFC and AE simulations are quantitatively consistent with each other. The discrepancy between these methods is about 1% in the interfacial energy and 5% in the surface stress which is the result of the truncation of higher harmonics of the density waves in the AE method. The values of the surface stress and the surface energy as well as the anisotropy parameters, $\alpha_f \equiv \frac{f(0^\circ)-f(30^\circ)}{f(0^\circ)+f(30^\circ)}$, are listed for the close-packed (0°) and the zigzag (30°) in Table I. Both PFC and AE exhibit weak anisotropy in the surface energy and larger anisotropy in the surface stress which suggests that the principal RLVs is the main determinant of the anisotropies. Moreover, for 2D hexagonal lattices, the maximum of surface energy/stress occurs at the close-packed surface while the minimum appears at the zigzag orientation.

We decompose the surface energy and the surface stress into the average value $\gamma^{(0)}(\tau_{tt}^{(0)})$ and its harmonics $\cos 6\theta$ and $\cos 12\theta$ according to Eqs. (11) and (12), and the coefficients are listed in Table II. The average surface stress $\tau_{tt}^{(0)}$ is 0.40% smaller than the average surface energy $\gamma^{(0)}$ in PFC simulation, while in AE simulation the difference increases to 2.66%. The discrepancy between the PFC model and the AE method once again is attributed to the truncation from the higher order

TABLE I. Surface free energy γ and stress τ_{tt} for two orientations at $\epsilon = 0.1$. α denotes the anisotropy parameter, which is defined as $\alpha_f \equiv \frac{f(0^\circ)-f(30^\circ)}{f(0^\circ)+f(30^\circ)}$.

	$\gamma(0^\circ)$ (10^{-4})	$\gamma(30^\circ)$ (10^{-4})	$\tau_{tt}(0^\circ)$ (10^{-4})	$\tau_{tt}(30^\circ)$ (10^{-4})	α_γ (%)	α_τ (%)
PFC	9.601	9.557	10.147	8.811	0.23	7.05
AE	9.524	9.483	9.644	8.349	0.22	7.20

TABLE II. The harmonics components of the surface stress and surface energy at $\epsilon = 0.1$.

	$\gamma^{(0)}$ (10^{-4})	$\gamma^{(6)}$ (10^{-4})	$\gamma^{(12)}$ (10^{-4})	$\tau_{tt}^{(0)}$ (10^{-4})	$\tau_{tt}^{(6)}$ (10^{-4})	$\tau_{tt}^{(12)}$ (10^{-4})
PFC	9.579	0.022	0.000	9.547	0.668	−0.065
AE	9.503	0.021	0.000	9.053	0.643	−0.057

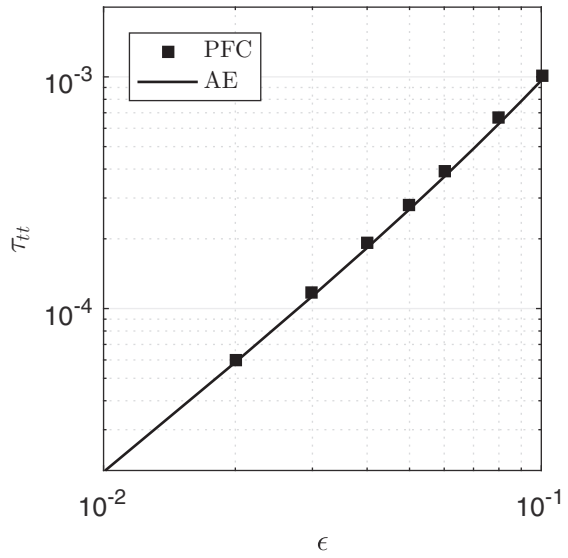

FIG. 8. The ϵ dependence of the surface stress for 0° orientations. The result of PFC simulation is shown in squares and the AE result is shown in the solid line.

modes in the density waves. Besides, τ_{tt} calculated in PFC and AE are plotted against ϵ in Fig. 8. The surface stress is shown to be proportional to $\epsilon^{3/2}$, as predicted by AE, and the discrepancy of τ measured from PFC and AE converges as ϵ decreases.

Similarly, the anisotropy calculated from the PFC and AE methods is in quantitatively good agreement for a wide range of ϵ as shown in Fig. 9, which suggests that the principal RLVs is the main determinant for the anisotropy. Both PFC and AE methods show that the surface stress is 30 times more anisotropic than the surface energy in the board range of ϵ from 0 to 0.1.

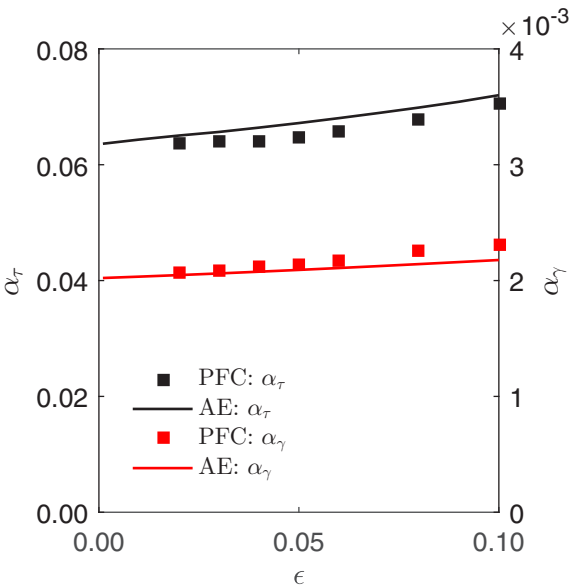

FIG. 9. The ϵ dependence of anisotropy parameters α of τ (black) and γ (red) is plotted for PFC (squares) and AE (lines) simulations.

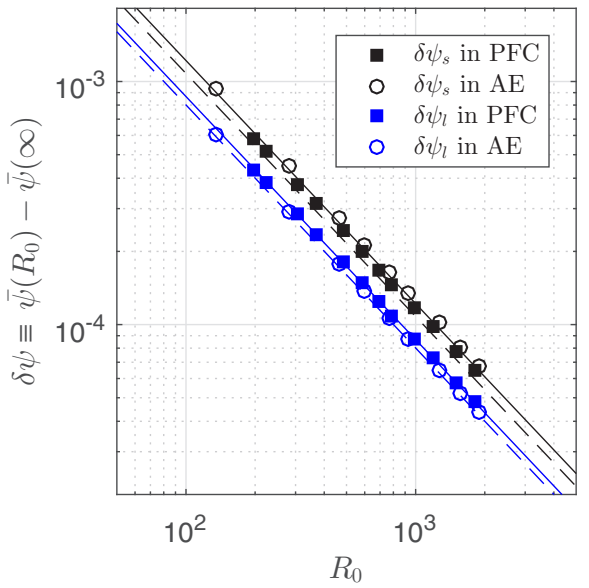

FIG. 10. The density shifts are measured in both phases and compared with the prediction of sharp interface model. The density variation for solid (liquid) is shown in black (blue). The simulation results from the PFC and the AE are depicted in squares and circles, respectively. The theoretical prediction in Eq. (54) is shown for PFC and AE in solid lines and dashed lines, respectively.

B. Circular crystal seeds

In this section, we employ both PFC and AE simulations to study the effect of the curved solid-liquid interface on the equilibrium state of nanoparticles. The simulation system consists of a circular solid embedded in the liquid phase and the radius of the circular solid is ranging from 20 to 280

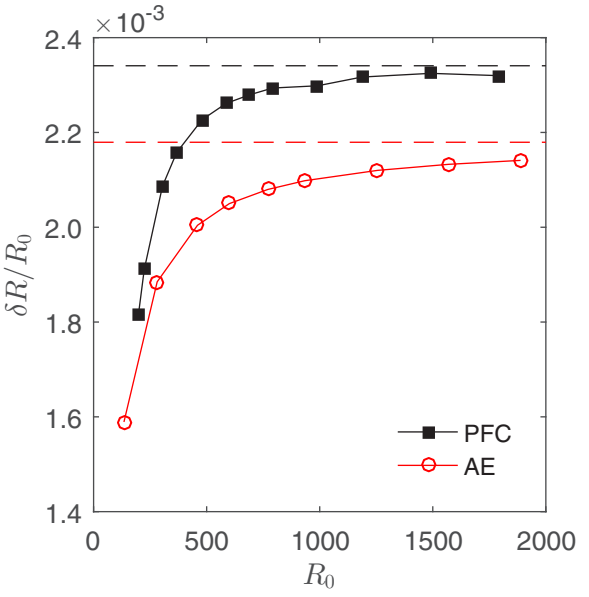

FIG. 11. The anisotropy of the equilibrium shape of various crystal size is plotted for PFC (squares) and AE (circles) simulations. The theoretical estimation of the shape anisotropy for large nanoparticles, $\alpha_R \cong \alpha_\gamma$, is shown in dashed lines.

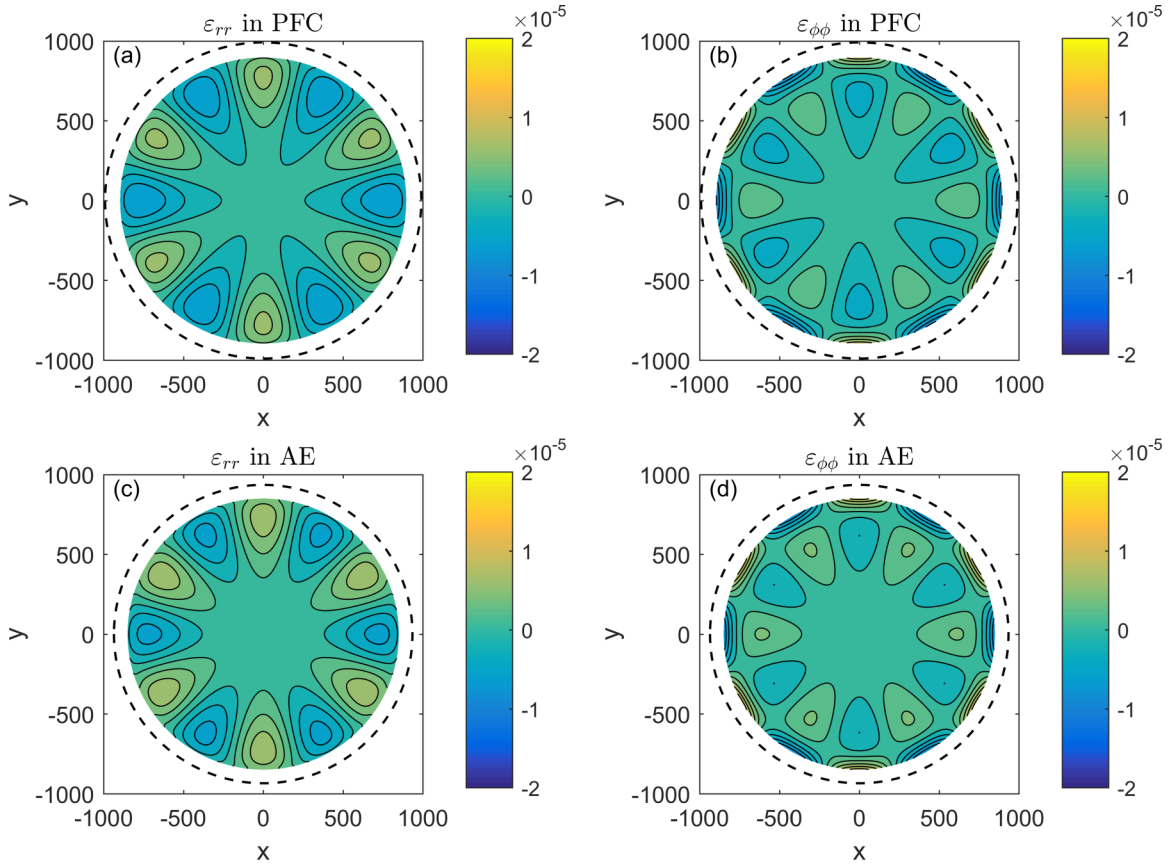

FIG. 12. The strains plot of (a) the radial and (b) the angular components for $R_0 = 991$ measured in PFC, and (c) the radial and (d) the angular components for $R_0 = 935$ calculated in AE. The dashed circle represents the position of interface. The strains are only plotted for the solid regime where the elastic moduli remain constant.

interatomic spacings in order to discern the effects of the surface stress between nanoparticles and large grains. We analyze in detail the shift of coexistence densities due to the curvature of nanoparticles and the noncircular equilibrium shape due to the anisotropic interfacial energy. Furthermore, we quantitatively compare numerical results of strain fields as a result of the intrinsic surface stress with the classical theory derived in Sec. II with assumptions of the sharp interface and linear elasticity. Inhomogeneous lattice distortion is observed within the crystal and its magnitude increases as the crystal size decreases.

1. Equilibrium density shift

In order to investigate elastic properties of nanoparticles quantitatively, one has to determine the equilibrium coexistence densities accurately since the elastic constants depend on the solid density and the Laplace pressure is calculated from the coexistence densities. The numerical results show that the coexistence mean densities increase as the radius of the crystal decreases as shown in Fig. 10. It is a direct result of the Gibbs-Thomson effect and the shift of the coexistence densities gives rise to the pressure difference between solid and liquid which balances the force due to the surface tension γ of the curved surface. The density shift $\delta\psi$ is defined as the difference in the density between solid-liquid systems with a curved and a planar interface, $\delta\psi_a \equiv \bar{\psi}_a(R_0) - \bar{\psi}_a(\infty)$, where a denotes either the solid ($a = s$) or the liquid ($a = \ell$) phase. The analytical expression for the density shift is obtained by solving Eqs. (3) and (4) together with the bulk free energy densities of PFC shown in Eqs. (19) and (22). The density shift is approximately

$$\delta\psi_a \cong \frac{\gamma}{f_a'' \Delta\psi R_0} + \mathcal{O}\left(R_0^{-2}\right), \tag{54}$$

where $\Delta\psi$ is the solid-liquid density difference for a planar solid-liquid interface system, $\Delta\psi \equiv \bar{\psi}_s - \bar{\psi}_l$, and f_a'' is the second derivative of free energy density with respect to the mean density, $f_a'' \equiv \partial^2 f/\partial\bar{\psi}_a^2$, which could be exactly calculated for liquid, $f_l'' = -\epsilon + 1 + 3\bar{\psi}_l^2$. Similar analytical derivation is carried out for AE by replacing $\bar{\psi}$ with $\epsilon^{3/2}n$ and using Eq. (32) for the bulk free energy density. As shown in Fig. 10, the simulation result is in good agreement with the theoretical calculation. The coexistence density shift is crucial for the following calculation of the surface stress, since it gives rise to the pressure difference acting on the interface which balances the surface stress.

2. Equilibrium shape

The equilibrium shape is crucial in computing the strains within a nanoparticle since one can no longer assume a circular boundary condition due to the anisotropic interfacial energy. The location of the interface is defined as that at which the mean density is equal to the average density of bulk solid and

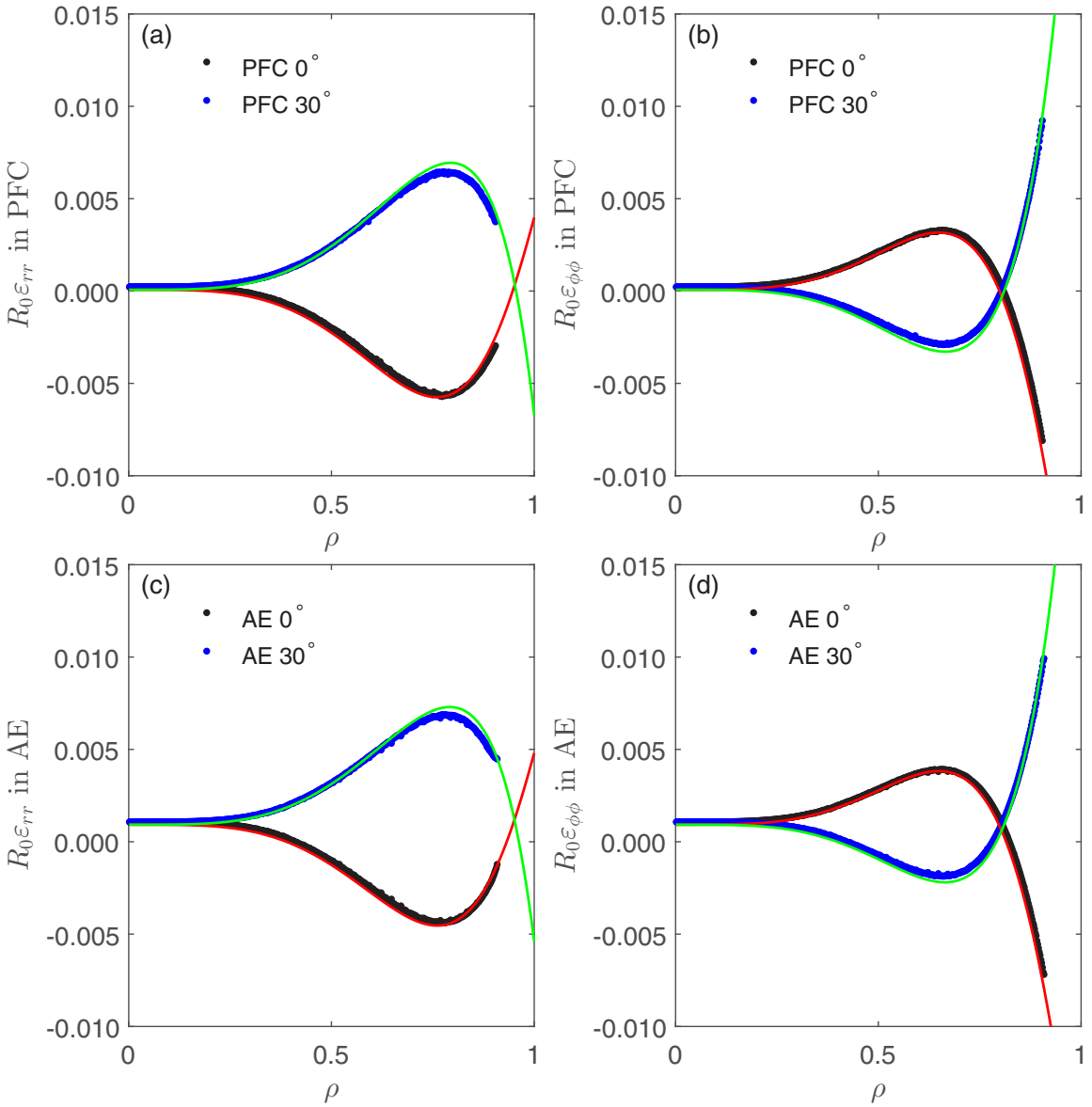

FIG. 13. The strain profiles of (a) the radial and (b) the angular components measured in PFC ($R_0 = 991$), and (c) the radial and (d) the angular components calculated in AE ($R_0 = 935$). The results are shown in black dots for the closed packed orientation (0°) and blue dots for the zigzag orientation (30°). The sharp interface prediction in Eqs. (13) and (14) is plotted in red lines for 0° and green lines for 30°.

liquid phases. Note that we employ the 2D Gaussian filter in PFC to smooth the density waves in solid to get the mean density profile. We measure the radius $R(\phi)$ and fit it with $R(\phi) \cong R_0 + \delta R \cos(6\phi)$. The equilibrium shape of the crystal seed is roughly circular and the radius variation, $\alpha_R \equiv \delta R/R_0$, is around 0.2% as shown in Fig. 11. For large nanoparticles, the radius variation can be estimated theoretically using Eq. (4),

$$\Delta p = \kappa(\gamma+\gamma'') \cong \frac{\gamma_0}{R_0}[(1-35\alpha_\gamma \cos 6\phi)(1+35\alpha_R \cos 6\phi)]. \tag{55}$$

Since the pressure difference must remain constant at equilibrium, it requires the above expression must be independent of ϕ. Therefore, the degree of the variation of radius is approximately equal to the anisotropy parameter of surface energy, $\alpha_R \cong \alpha_\gamma$. The simulation results are quantitatively consistent with the theoretical value for crystal seeds with a large radius, see Fig. 11. However, the equilibrium shape is shown to be more isotropic as the radius of the crystal becomes smaller, which indicates a curvature dependent surface energy and its anisotropy.

3. Strain profiles

In order to examine the effect of the surface stress, we investigate strain fields within the solid. In PFC simulations, we calculate the displacement $\vec{u}$ by measuring the location of each density peak and subtracting it by that of a stress-free solid. On the other hand, in AE simulations, we measure the phase of the amplitudes and determine the displacement field based on Eq. (36). For both PFC and AE, the displacement field is only measured within the nanoparticles where the elastic moduli are constants.

The strain fields are defined as the symmetrized displacement gradient, $\varepsilon_{\alpha\beta} = \frac{1}{2}(u_{\alpha,\beta} + u_{\beta,\alpha})$. The resulting diagonal components of strains is shown in Fig. 12, and the strain fields exhibit strong orientation dependence. For the radial component ε_{rr}, the material is compressed along the close-packed orientation and stretched along the zigzag orientation. In contrast to radial component, the angular component exhibits a more complex behavior in that the region close to the interface of the crystal is compressed in the close-packed orientation and stretched in the zigzag orientation, while the relation is reversed for regions that are away from the interface. As shown in Fig. 13, the strain profile within the solid is in good agreement with the sharp-interface prediction derived in Eqs. (13) and (14). The small deviation in ε_{rr} near the peak is a result of the simple theoretical assumption of a circular equilibrium shape. As shown previously, a weak noncircular shape is presented in the PFC and AE due to the anisotropic surface energy.

To further compare strain fields quantitatively with Eqs. (13)–(15), we decompose the measured strain fields into a sum of isotropic terms and the first harmonics,

$$\varepsilon_{rr}(r,\phi) \cong \varepsilon_{rr}^{(0)}(r) + \varepsilon_{rr}^{(6)}(r)\cos(6\phi) \tag{56}$$

$$\varepsilon_{\phi\phi}(r,\phi) \cong \varepsilon_{\phi\phi}^{(0)}(r) + \varepsilon_{\phi\phi}^{(6)}(r)\cos(6\phi) \tag{57}$$

$$\varepsilon_{\phi r}(r,\phi) \cong \varepsilon_{\phi r}^{(6)}(r)\sin(6\phi), \tag{58}$$

where $\varepsilon_{ij}^{(0)}$ and $\varepsilon_{ij}^{(6)}$ only depend on the radial coordinate. It is clear that, from Eqs. (13)–(15), $\varepsilon_{ij}^{(6m)}$ is related to $\gamma^{(6m)}$ and $\tau^{(6m)}$ and is inversely proportional to R_0.

From Eqs. (13) and (14), we expect the isotropic strains to be the same value within the solid, $\varepsilon_{rr}^{(0)} = \varepsilon_{\phi\phi}^{(0)} = \frac{\Delta\tau_{tt}^{(0)}}{2KR_0}$. The isotropic strains measured from simulations are compared with classical theory in Fig. 14. The simulation result is consistent with theory for large nanoparticles that the isotropic strains change inversely with R_0; the minor deviation for large nanoparticles can be attributed to the noncircular equilibrium shape. However, for smaller nanoparticles, the isotropic strains dramatically deviate from sharp interface prediction which suggests that $\Delta\tau_{tt}^{(0)} = \tau_{tt}^{(0)} - \gamma^{(0)} = \tau_{tt}^{(0)} - R_0\Delta p$ is no longer a constant. With the result in density shift corresponding to the pressure difference, the simulation results of PFC and AE indeed show a pronounced reduction in the average surface stress as the size of the nanoparticle decreases and insignificant changes in $R_0\Delta p$. For the nanoparticle size $R_0 \cong 282$ in AE, for example, the changes in $R_0\Delta p$ is about 0.4% and τ changes by 1.5%. Therefore, the decrease in the surface stress results in a decrease in the isotropic strains.

Besides, the coefficients of the first harmonics of strains are plotted against the radial position in Fig. 15. The dependence of the first harmonics coefficient on r is in quantitatively good agreement with theory for large nanoparticles; however, the deviation appears for small nanoparticles. To understand the physical origin of the deviation, we fit the measured strain fields with the general solution of an isotropic elastic material. Despite the complexity of the diffusive interface and the noncircular equilibrium shape, at mechanical equilibrium, the general solution of the displacement field expressed in the polar coordinates can be derived as shown in Appendix A. With the displacement field, one can readily derive the general form of the strain fields and $\varepsilon_{\alpha\beta}^{(6)}$ accordingly,

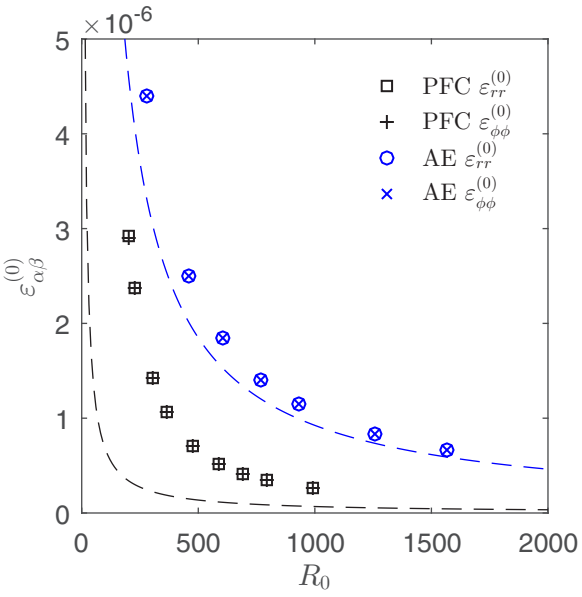

FIG. 14. The bulk strain $\varepsilon_{\alpha\beta}^{(0)}$ of the PFC (black) and the AE (blue) simulations is compared with the prediction by the sharp interface theory in Eq. (10) which are plotted in dashed lines.

$$R_0\varepsilon_{rr}^{(6)} = a_{rr}^{(6)}\rho^6 + b_{rr}^{(6)}\rho^4 \tag{59}$$

$$R_0\varepsilon_{\phi\phi}^{(6)} = a_{\phi\phi}^{(6)}\rho^6 + b_{\phi\phi}^{(6)}\rho^4 \tag{60}$$

$$R_0\varepsilon_{\phi r}^{(6)} = \left(\frac{-a_{rr}^{(6)} + a_{\phi\phi}^{(6)}}{2}\right)\rho^6 + \left(\frac{-2b_{rr}^{(6)} + b_{\phi\phi}^{(6)}}{3}\right)\rho^4, \tag{61}$$

where $a_{\alpha\beta}^{(6)}$ and $b_{\alpha\beta}^{(6)}$ are constant coefficients independent of r and ϕ. For sharp interface theory, $a_{\alpha\beta}^{(6)}$ and $b_{\alpha\beta}^{(6)}$ are independent of R_0, which leads to a unique profile of $R_0\varepsilon_{\alpha\beta}^{(6)}$ regardless of the nanoparticles size. By contrast, in PFC and AE, these coefficients are shown to depend on the curvature. However, these curvature dependent coefficients do not affect the shape of the profile of $R_0\varepsilon_{\alpha\beta}^{(6)}$, but only reduce the magnitude of the profiles as R_0 decreases. It indicates that the surface stress of a diffusive interface depends on the size of the nanoparticle. It is of interest to estimate the effective surface stress which gives rise to the corresponding strain fields observed in PFC and AE simulations.

4. *Effective surface stress*

The effective surface stress is defined as the surface stress required to act on the noncircular shape surface that leads to the measured strain fields. Therefore, based on the validity of the isotropic linear elasticity, we use the strain fields within the solid to extrapolate the strain fields at the interface using Eqs. (59)–(61). The effective surface stress is readily evaluated using the extrapolated strains at the interface and Eq. (7) with the pressure difference calculated from the density shift. The

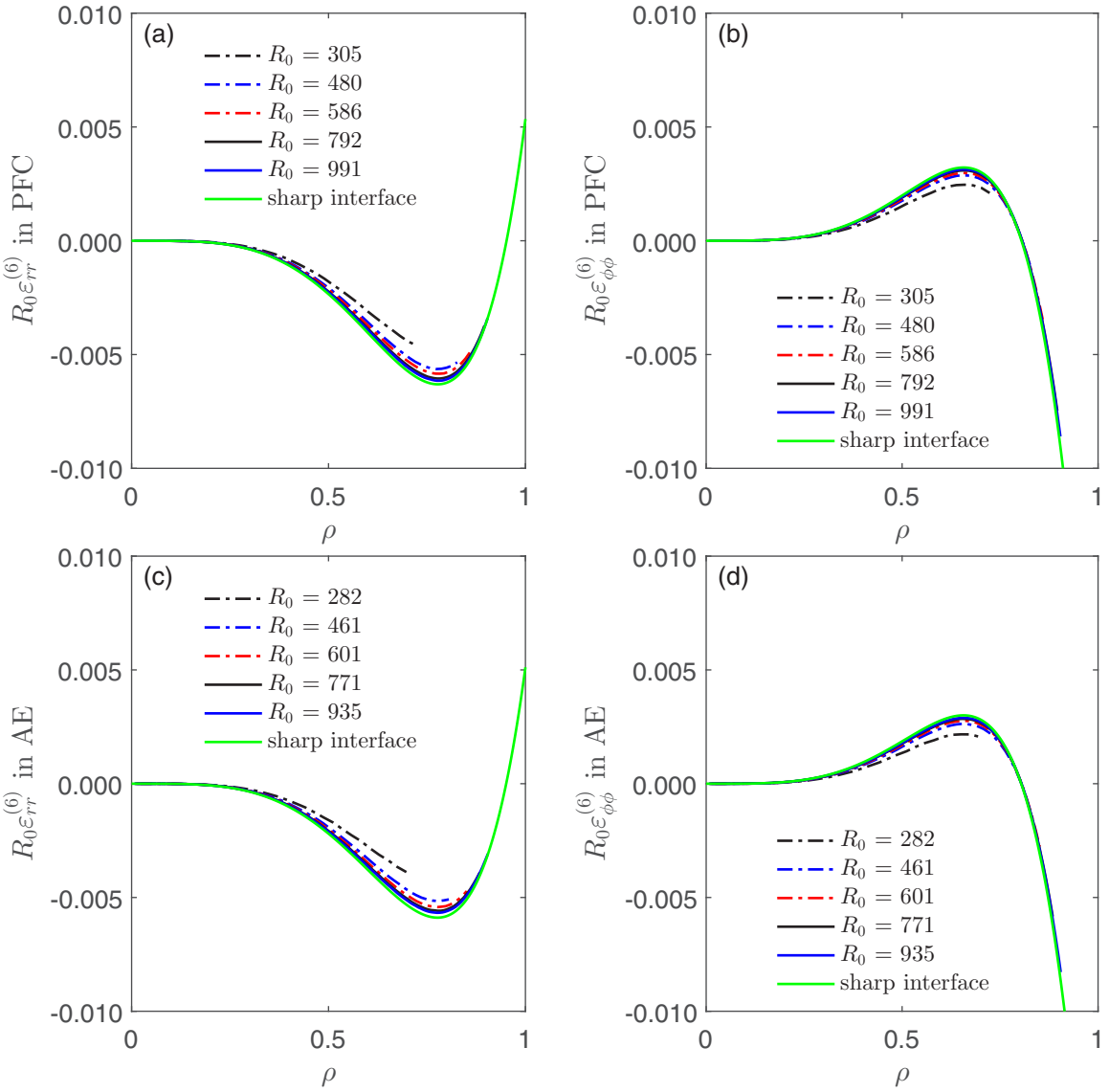

FIG. 15. The profiles of the first harmonics of (a) the radial and (b) the angular strain components measured from PFC simulations, and (c) the radial and (d) the angular components calculated in AE method. The green line is the prediction by sharp interface theory in Eqs. (13) and (14).

sharp interface theory does correctly predict the $\tau_{tt}^{(0)}$ and $\tau_{tt}^{(6)}$ for large nanoparticles, see Fig. 16; however, the effective surface stress deviates from the sharp interface theory as the curvature of the interface increases. Both the average and the anisotropy of the effective surface stress are reduced as the radius of the nanoparticle decreases. In particular, the anisotropy of the effective surface stress exhibits strong dependence on the size of the nanoparticle. The weaker anisotropy in the surface stress for smaller nanoparticles is related to the fact that amplitudes of density waves decay into liquid across a finite width of a diffusive interface. And as the curvature of the nanoparticle increases, the interfacial area has the shape of a sector of a circular ring. Therefore, in the calculation of the surface stress for a given orientation, the surface stress would contain information of density waves from nearby orientation. Hence, the anisotropy of the surface is reduced.

V. CONCLUSION

We employ the PFC and AE approaches to investigate the properties of the surface stress of diffusive solid-liquid interfaces. Using the AE formalism, the free energy functional is recast in terms of the strain field and the magnitude of amplitudes of density waves, which sheds light on the intricate coupling between the density waves and strains across the solid-liquid diffusive interface. The derived expression is helpful in constructing phenomenological models such as the phase field that describes realistic surface stress of a diffusive interface [57,59,60]. In addition, we show a strain-dependent excess interfacial energy which leads to surface stress that is consistent with the Shuttleworth relation. To quantitatively investigate the surface stress and its anisotropy, we calculate the surface stress of a planar interface for different crystal orientation using both PFC and AE. The result shows that

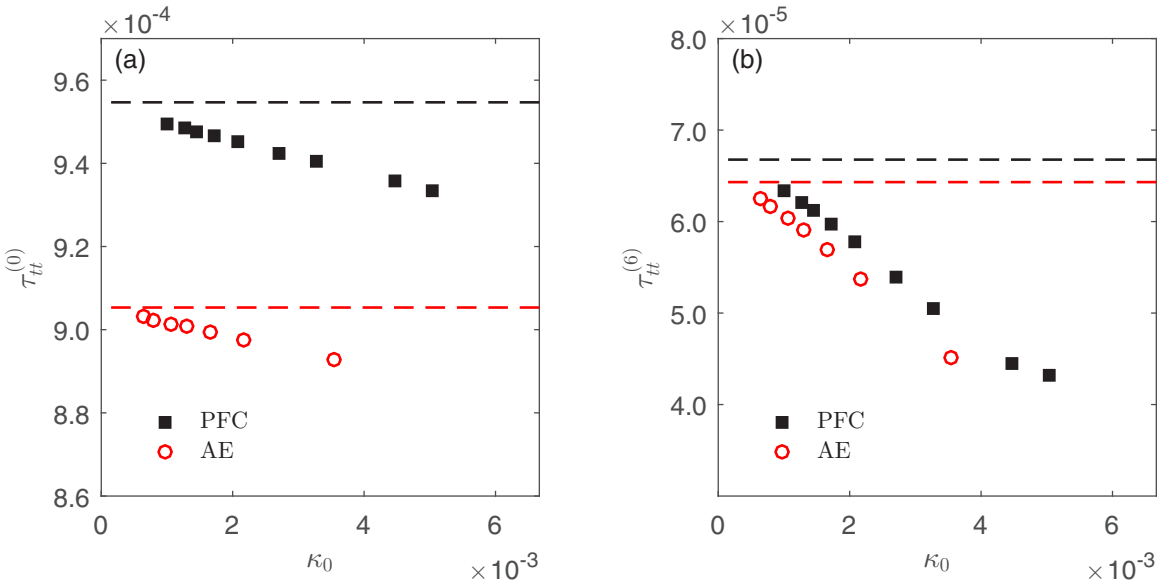

FIG. 16. (a) The average value and (b) the first harmonics of effective surface stress in seed simulation is compared with the sharp interface theory. The simulation result is shown in black squares for PFC and red circles for AE, and the prediction is shown in a dashed line. The mean curvature κ_0 is defined as $\kappa_0 \equiv 1/R_0$.

the surface stress is always compressive regardless of the orientation for 2D hexagonal-liquid interface in the PFC model and it is substantially more anisotropic than the surface energy for a wide range of the control parameter ϵ. It is expected that the pronounced anisotropy in the surface stress would influence the equilibrium state of the crystal, in particular, at the nanoparticles. Therefore, we analyze the effect due to the surface stress on a nanoparticle immersed in its liquid phase. We study the resultant strain fields within the solid in the numerical simulations and compare them with the theoretical predictions based on the classical sharp interface model. In order to make quantitative comparison, we have to take into account the coexistence density shift due to the Gibbs-Thomson effect and noncircular equilibrium shape due to anisotropic surface energy. With the information of coexistence density and the equilibrium shape, we readily compare the strain fields measured in simulations with the sharp interface model. The profiles of strains in simulations are in quantitatively good agreement with the prediction for large nanoparticles. As the size decreases, however, the strain profiles deviate from the classical prediction which suggests the surface stress of nanoparticle is different than that of a planer interface. We identify that, for small nanoparticles, the bulk strain rises and the strain fields become more isotropic. Using the measured strain fields, we reconstruct an effective surface stress. Both the average and the anisotropy of the effective surface stress decrease as the curvature of the interface increases. The weaker anisotropy in the effective surface stress for small nanoparticles is due to the fact that the profiles of density waves across a curved interface are related to multiple interface normals in contrast to a unique interface normal for the planar case.

ACKNOWLEDGMENTS

The authors thank M. P. Gururajan for helpful discussions. We gratefully acknowledge the support of the Ministry of Science and Technology, Taiwan (Grant No. MOST 105-2112-M-007-031-MY3), and the support from National Center for Theoretical Sciences, Taiwan.

APPENDIX A: EQUILIBRIUM STRAIN PROFILES IN POLAR COORDINATES

In polar coordinates (r,ϕ), the deformation gradient $u_{\alpha,\beta}$ is expressed in terms of displacement field (u_r,u_ϕ),

$$u_{r,r} = \partial_r u_r \qquad u_{\phi,r} = \partial_r u_\phi$$
$$u_{r,\phi} = \frac{1}{r}(\partial_\phi u_r - u_\phi) \qquad u_{\phi,\phi} = \frac{1}{r}(\partial_\phi u_\phi + u_r), \tag{A1}$$

where $\partial_\alpha \equiv \frac{\partial}{\partial \alpha}$. The corresponding strain field $\varepsilon_{\alpha\beta}$ is calculated accordingly using $\varepsilon_{\alpha\beta} = \frac{1}{2}(u_{\alpha,\beta} + u_{\beta,\alpha})$.

For the isotropic linear elastic material, the mechanical equilibrium condition, $\nabla \cdot \boldsymbol{\sigma} = 0$, is readily rewritten into a second order partial differential equation of $\vec{u}$,

$$\tfrac{1}{2}(K+G)\nabla(\nabla\cdot\vec{u}) + G(\nabla^2\vec{u}) = 0, \tag{A2}$$

where $\nabla = \hat{r}\partial_r + \hat{\phi}\frac{1}{r}\partial_\phi$ in polar coordinates. The general solution for Eq. (A2) is obtained straightforwardly,

$$u_r(r,\phi) = a_r^{(0)} r + \sum_{m=1}^{\infty}\left[a_r^{(m)} r^{m+1} + b_r^{(m)} r^{m-1}\right]\cos(m\phi) \tag{A3}$$

$$u_\phi(r,\phi) = \sum_{m=1}^{\infty}\left[a_\phi^{(m)} r^{m+1} + b_\phi^{(m)} r^{m-1}\right]\sin(m\phi), \tag{A4}$$

where $a_r^{(0)}$, $a_\alpha^{(m)}$, and $b_\alpha^{(m)}$ are independent of r and ϕ. Consequently, the strain fields become

$$R_0\varepsilon_{rr} = a_{rr}^{(0)} + \sum_{m=1}^{\infty}\left[a_{rr}^{(m)}\rho^m + b_{rr}^{(m)}\rho^{m-2}\right]\cos(m\phi) \quad \text{(A5)}$$

$$R_0\varepsilon_{\phi\phi} = a_{rr}^{(0)} + \sum_{m=1}^{\infty}\left[a_{\phi\phi}^{(m)}\rho^m + b_{\phi\phi}^{(m)}\rho^{m-2}\right]\cos(m\phi) \quad \text{(A6)}$$

$$R_0\varepsilon_{\phi r} = \sum_{m=1}^{\infty}\left[\left(\frac{-a_{rr}^{(m)} + a_{\phi\phi}^{(m)}}{2}\right)\rho^m + \left(\frac{-(m+2)b_{rr}^{(m)} + (m-2)b_{\phi\phi}^{(m)}}{2m}\right)\rho^{m-2}\right]\sin(m\phi), \quad \text{(A7)}$$

where $\rho \equiv \frac{r}{R_0}$ and R_0 is the radius of the nanoparticle. The relations between the coefficients of $\varepsilon_{\alpha\beta}$ and that of u_α are

$$a_{rr}^{(0)} = R_0 a_r^{(0)} \quad \text{(A8)}$$

$$a_{rr}^{(m)} = R_0^m(m+1)a_r^{(m)} \quad \text{(A9)}$$

$$a_{\phi\phi}^{(m)} = R_0^m\left(a_r^{(m)} + m a_\phi^{(m)}\right) \quad \text{(A10)}$$

$$b_{rr}^{(m)} = R_0^{m-2}(m-1)b_r^{(m)} \quad \text{(A11)}$$

$$b_{\phi\phi}^{(m)} = R_0^{m-2}\left(b_r^{(m)} + m b_\phi^{(m)}\right). \quad \text{(A12)}$$

For a circular seed with a sharp interface, using the mechanical equilibrium equation at the interface, Eq. (7), as well as the constitutive relation in Eq. (9), we obtain the coefficients in terms of the surface energy, surface stress, and the elastic moduli,

$$a_{rr}^{(0)} = -\frac{1}{2K}\left(\tau_{tt}^{(0)} - \gamma^{(0)}\right) \quad \text{(A13)}$$

$$a_{rr}^{(m)} = -(m+1)\left(\frac{1}{2K} - \frac{m}{4G}\right)\left(\tau_{tt}^{(m)} + (m-1)\gamma^{(m)}\right) \quad \text{(A14)}$$

$$a_{\phi\phi}^{(m)} = -(m+1)\left(\frac{1}{2K} + \frac{m}{4G}\right)\left(\tau_{tt}^{(m)} + (m-1)\gamma^{(m)}\right) \quad \text{(A15)}$$

$$b_{rr}^{(m)} = -(m-1)\left(\frac{m}{4G}\right)\left(\tau_{tt}^{(m)} + (m+1)\gamma^{(m)}\right) \quad \text{(A16)}$$

$$b_{\phi\phi}^{(m)} = (m-1)\left(\frac{m}{4G}\right)\left(\tau_{tt}^{(m)} + (m+1)\gamma^{(m)}\right), \quad \text{(A17)}$$

where $\tau_{tt}^{(0)}$ and $\tau_{tt}^{(m)}$ are the isotropic term and the Fourier component, respectively, of the surface stress.

APPENDIX B: ELASTIC MODULI

As derived above, M_j, a scalar proportional to $\varepsilon_{\alpha\beta}$, plays a crucial role in the mechanical equilibrium conditions in bulk solid of which the free energy density is associated with strains, $\bar{f}_s = \sum_{j=1}^{3} M_j^2 a_j^2 + \bar{f}_{\text{local}}$. The stress-strain relation could be derived by calculating the first derivative of the solid free energy density with respect to $\varepsilon_{\alpha\beta}$,

$$\begin{aligned}\sigma_{\alpha\beta} &\equiv \epsilon^2\left(-\bar{p}_s\delta_{\alpha\beta} + \frac{\partial \bar{f}_s}{\partial \varepsilon_{\alpha\beta}}\right)\\ &\cong -\epsilon^2\bar{p}_s\delta_{\alpha\beta} + \epsilon^2\sum_{j=1}^{3} 2M_j\frac{\partial M_j}{\partial \varepsilon_{\alpha\beta}}a_j^2 + \mathcal{O}(\varepsilon^2)\\ &= -\epsilon^2\bar{p}_s\delta_{\alpha\beta} + \epsilon\sum_{j=1}^{3} 8a_j^2 K_{j\alpha}K_{j\beta}K_{j\mu}K_{j\nu}\varepsilon_{\mu\nu},\end{aligned} \quad \text{(B1)}$$

where $\bar{p}_s \equiv n_s\left(\frac{\partial \bar{f}_s}{\partial n_s}\right) - \bar{f}_s$. The corresponding stiffness tensor $C_{\alpha\beta\mu\nu}$ is calculated according to $\sigma_{\alpha\beta} = C_{\alpha\beta\mu\nu}\varepsilon_{\mu\nu}$,

$$C_{\alpha\beta\mu\nu} = 8\epsilon\bar{A}^2\sum_{j=1}^{3} K_{j\alpha}K_{j\beta}K_{j\mu}K_{j\nu}, \quad \text{(B2)}$$

where $\bar{A}$ is the equilibrium solid amplitude. Note that this relation could be generalized to any lattice structure and the resultant elastic moduli only depend on the group of RLVs. For d-dimensional materials, the Poisson's ratio, $\nu \equiv \frac{C_{1122}}{C_{1111}+(d-2)C_{1122}}$, and the Zener anisotropy ratio, $a_r \equiv \frac{2C_{1212}}{C_{1111}-C_{1122}}$, exclusively depend on the principal RLVs which reflect the underlying symmetry, see Table III. Our results are consistent with that shown by Elder *et al.* [38]. For crystal structures formed by multiple sets of RLVs, one can generalize Eq. (B2) to evaluate the stiffness tensor.

For triangular lattices, the principal RLVs are defined in Eq. (21), the summation $\sum_{j=1}^{3} K_{j\alpha}K_{j\beta}K_{j\mu}K_{j\nu}$ equals to $\frac{3}{8}(\delta_{\alpha\beta}\delta_{\mu\nu} + \delta_{\alpha\mu}\delta_{\beta\nu} + \delta_{\alpha\nu}\delta_{\beta\mu})$, which leads to the isotropic elastic moduli,

$$\begin{aligned}C_{\alpha\beta\mu\nu} &= 3\epsilon\bar{A}^2(\delta_{\alpha\beta}\delta_{\mu\nu} + \delta_{\alpha\mu}\delta_{\beta\nu} + \delta_{\alpha\nu}\delta_{\beta\mu})\\ &= (6\epsilon\bar{A}^2)\delta_{\alpha\beta}\delta_{\mu\nu} + 2(3\epsilon\bar{A}^2)\left(\delta_{\alpha\mu}\delta_{\beta\nu} - \frac{1}{2}\delta_{\alpha\beta}\delta_{\mu\nu}\right).\end{aligned} \quad \text{(B3)}$$

Based on Eqs. (9) and (B3), the bulk and shear moduli as well as the isotropic pressure are calculated directly, $K = 6\epsilon\bar{A}^2 \cong 6A_s^2$, $G = 3\epsilon\bar{A}^2 \cong 3A_s^2$ and $p_s = \epsilon^2\bar{p}_s$.

TABLE III. The list of the stiffness tensor $C_{\alpha\beta\mu\nu}$ and elastic moduli including Young's modulus Y, the bulk modulus K, the shear modulus G, the Poisson's ratio ν, and the Zener anisotropy ratio a_r for the 2D triangular lattice and the 3D body centered cubic crystal. Note that $\epsilon\bar{A}^2$ corresponds to A_s^2 in the PFC description.

Crystal structure	C_{1111}	C_{1122}	C_{1212}	Y	K	G	ν	a_r
2D triangular	$9\epsilon\bar{A}^2$	$3\epsilon\bar{A}^2$	$3\epsilon\bar{A}^2$	$8\epsilon\bar{A}^2$	$6\epsilon\bar{A}^2$	$3\epsilon\bar{A}^2$	$\frac{1}{3}$	1
3D BCC	$8\epsilon\bar{A}^2$	$4\epsilon\bar{A}^2$	$4\epsilon\bar{A}^2$	$\frac{16}{3}\epsilon\bar{A}^2$	$\frac{16}{3}\epsilon\bar{A}^2$	$4\epsilon\bar{A}^2$	$\frac{1}{3}$	2

[1] J. Zang, M. Huang, and F. Liu, Phys. Rev. Lett. **98**, 146102 (2007).
[2] K. G. Kornev and D. J. Srolovitz, Appl. Phys. Lett. **85**, 2487 (2004).
[3] H. Ibach, Surf. Sci. Rep. **29**, 195 (1997).
[4] R. J. Needs, M. J. Godfrey, and M. Mansfield, Surf. Sci. **242**, 215 (1991).
[5] D. Wolf, Phys. Rev. Lett. **70**, 627 (1993).
[6] W. Lu and Z. Suo, J. Mech. Phys. Solids **49**, 1937 (2001).
[7] W. Lu and Z. Suo, Phys. Rev. B **65**, 205418 (2002).
[8] W. Lu and D. Kim, Nano Lett. **4**, 313 (2004).
[9] J. A. Floro, E. Chason, R. C. Cammarata, and D. J. Srolovitz, MRS Bull. **27**, 19 (2011).
[10] J. W. Gibbs, *The Collected Works of J. Willard Gibbs* (Longmans, Green, New York, 1928), p. 2 v.
[11] R. C. Cammarata, Prog. Surf. Sci. **46**, 1 (1994).
[12] R. Shuttleworth, Proc. Phys. Soc. London, Sect. A **63**, 444 (1950).
[13] J. Q. Broughton and G. H. Gilmer, Acta Metall. **31**, 845 (1983).
[14] P. Gumbsch and M. S. Daw, Phys. Revi. B **44**, 3934 (1991).
[15] W. Jun, Y. L. Fan, D. W. Gong, S. G. Shen, and X. Q. Fan, Modell. Simul. Mater. Sci. Eng. **7**, 189 (1999).
[16] Q. Jiang, L. H. Liang, and D. S. Zhao, J. Phys. Chem. B **105**, 6275 (2001).
[17] V. B. Shenoy, Phys. Rev. B **71**, 094104 (2005).
[18] T. Frolov and Y. Mishin, Phys. Rev. B **79**, 045430 (2009).
[19] T. Frolov and Y. Mishin, Modell. Simul. Mater. Sci. Eng. **18**, 074003 (2010).
[20] T. Frolov and Y. Mishin, Phys. Rev. B **82**, 174114 (2010).
[21] K. R. Elder, N. Provatas, J. Berry, P. Stefanovic, and M. Grant, Phys. Rev. B **75**, 064107 (2007).
[22] K. R. Elder, M. Katakowski, M. Haataja, and M. Grant, Phys. Rev. Lett. **88**, 245701 (2002).
[23] K. R. Elder and M. Grant, Phys. Rev. E **70**, 051605 (2004).
[24] N. Pisutha-Arnond, V. W. L. Chan, K. R. Elder, and K. Thornton, Phys. Rev. B **87**, 014103 (2013).
[25] V. Heinonen, C. V. Achim, K. R. Elder, S. Buyukdagli, and T. Ala-Nissila, Phys. Rev. E **89**, 032411 (2014).
[26] K.-A. Wu and P. W. Voorhees, Phys. Rev. B **80**, 125408 (2009).
[27] Y.-M. Yu, R. Backofen, and A. Voigt, J. Cryst. Growth **318**, 18 (2011).
[28] M. A. Choudhary, J. Kundin, and H. Emmerich, Comput. Mater. Sci. **83**, 481 (2014).
[29] F. Podmaniczky, G. I. Tóth, G. Tegze, and L. Gránásy, Metall. Mater. Trans. A **46**, 4908 (2015).
[30] F. Podmaniczky, G. I. Tóth, G. Tegze, T. Pusztai, and L. Gránásy, J. Cryst. Growth **457**, 24 (2017).
[31] R. Backofen and A. Voigt, J. Phys.: Condens. Matter **22**, 364104 (2010).
[32] G. I. Tóth, G. Tegze, T. Pusztai, G. Tóth, and L. Gránásy, J. Phys.: Condens. Matter **22**, 364101 (2010).
[33] L. Gránásy, G. Tegze, G. I. Tóth, and T. Pusztai, Philos. Mag. **91**, 123 (2011).
[34] S. Tang, Y. M. Yu, J. Wang, J. Li, Z. Wang, Y. Guo, and Y. Zhou, Phys. Rev. E **89**, 012405 (2014).
[35] T. Yang, Z. Chen, J. Zhang, Y. Wang, and Y. Lu, Chin. Phys. B **25**, 038103 (2016).
[36] S. Tang, J. Wang, J. Li, Z. Wang, Y. Guo, C. Guo, and Y. Zhou, Phys. Rev. E **95**, 062803 (2017).
[37] S.-C. Lin, M.-W. Liu, M. P. Gururajan, and K.-A. Wu, Acta Mater. **102**, 364 (2016).
[38] K. R. Elder, Z. F. Huang, and N. Provatas, Phys. Rev. E **81**, 011602 (2010).
[39] Z. F. Huang, K. R. Elder, and N. Provatas, Phys. Rev. E **82**, 021605 (2010).
[40] H. Löwen, J. Phys.: Condens. Matter **22**, 364105 (2010).
[41] R. Wittkowski, H. Lowen, and H. R. Brand, Phys. Rev. E **82**, 031708 (2010).
[42] M. Seymour, F. Sanches, K. Elder, and N. Provatas, Phys. Rev. B **92**, 184109 (2015).
[43] N. Goldenfeld, B. P. Athreya, and J. A. Dantzig, Phys. Rev. E **72**, 020601 (2005).
[44] B. P. Athreya, N. Goldenfeld, and J. A. Dantzig, Phys. Rev. E **74**, 011601 (2006).
[45] K.-A. Wu and A. Karma, Phys. Rev. B **76**, 184107 (2007).
[46] Z. F. Huang and K. R. Elder, Phys. Rev. Lett. **101**, 158701 (2008).
[47] R. Spatschek and A. Karma, Phys. Rev. B **81**, 214201 (2010).
[48] D.-H. Yeon, Z.-F. Huang, K. R. Elder, and K. Thornton, Philos. Mag. **90**, 237 (2010).
[49] P. K. Galenko, F. I. Sanches, and K. R. Elder, Physica D: Nonlinear Phenomena **308**, 1 (2015).
[50] P. Y. Chan and N. Goldenfeld, Phys. Rev. E **80**, 065105 (2009).
[51] C. Hüter, M. Friák, M. Weikamp, J. Neugebauer, N. Goldenfeld, B. Svendsen, and R. Spatschek, Phys. Rev. B **93**, 214105 (2016).
[52] Z.-F. Huang and K. R. Elder, Phys. Rev. B **81**, 165421 (2010).
[53] K. A. Wu, A. Adland, and A. Karma, Phys. Rev. E **81**, 061601 (2010).
[54] M. Greenwood, N. Provatas, and J. Rottler, Phys. Rev. Lett. **105**, 045702 (2010).
[55] M. Greenwood, J. Rottler, and N. Provatas, Phys. Rev. E **83**, 031601 (2011).
[56] R. L. Davidchack and B. B. Laird, J. Chem. Phys. **108**, 9452 (1998).
[57] V. I. Levitas, Phys. Rev. B **87**, 054112 (2013).
[58] J. Mellenthin, A. Karma, and M. Plapp, Phys. Rev. B **78**, 184110 (2008).
[59] V. I. Levitas and K. Samani, Nat. Commun. **2**, 284 (2011).
[60] V. I. Levitas and J. A. Warren, J. Mech. Phys. Solids **91**, 94 (2016).